

# Learning Dynamic Structural Specialization for Underwater Salient Object Detection

Lin Hong, *Member, IEEE*, Chenhui Wang, Linan Deng, Yuning Cui, Yu Zhang, Xin Wang, *Member, IEEE*, Bojian Zhang, Wenqi Ren, *Senior Member, IEEE*, Xingchen Yang, and Fumin Zhang, *Fellow, IEEE*

**Abstract**—Underwater salient object detection (USOD) has attracted increasing attention for underwater visual scene understanding and vision-guided robotic applications. However, existing USOD methods still struggle with underwater image degradations, which often lead to inaccurate object localization, fragmented salient regions, and coarse boundary prediction. To address these challenges, this paper proposes DSS-USOD, a novel RGB-based USOD method built upon dynamic structural specialization. DSS-USOD extracts a shared base representation from a single underwater image, decomposes it into boundary-sensitive and region-coherent structural features, and dynamically coordinates their contributions according to local structural context. Specifically, the extracted shared base representation is decomposed into a boundary-sensitive branch for modeling fine-grained boundary details and a region-coherent branch for capturing region-level structural consistency. A spatial coordination module is then introduced to adaptively regulate the relative contributions of the two branches according to local structural context. Moreover, cooperative structural supervision is introduced to promote branch specialization and stabilize spatial coordination, enabling DSS-USOD to better balance boundary precision and region coherence under degraded underwater conditions. Extensive experiments show that DSS-USOD achieves superior performance on benchmark datasets. Finally, real-world deployment on an underwater robot validates the practical effectiveness of DSS-USOD for underwater object inspection. The code and models are publicly available at <https://github.com/LinHong-HIT/DSS-USOD>.

**Index Terms**—Underwater salient object detection, dynamic structural specialization, boundary-region entanglement, dynamic coordination

## I. INTRODUCTION

IN visual scene understanding, accurately identifying visually important structures from uncertain and degraded sensory observations is a fundamental yet challenging problem [1]. Underwater salient object detection (USOD) instantiates this problem by localizing and segmenting visually distinctive objects in complex underwater scenarios [2], [3]. As

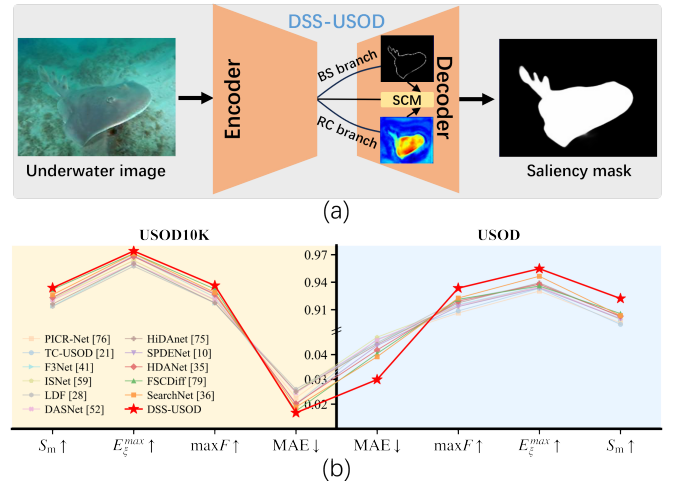


Fig. 1. (a) Overview of dynamic structural specialization design in DSS-USOD. (b) Quantitative comparison with representative SOTA methods on the USOD10K and USOD, DSS-USOD consistently achieves superior performance across four evaluation metrics on both datasets.

a fundamental task in underwater visual scene understanding, USOD has been widely studied and plays an important role in various vision-guided robotic applications, including marine environmental monitoring [4], underwater benthic surveys [5], and underwater infrastructure inspection [6], [7]. However, unlike terrestrial imagery, underwater images are often severely degraded by light absorption and scattering, which lead to color distortion, low contrast, and noise interference [8], [9]. These degradations weaken the stability and reliability of visual cues, making accurate and stable salient object detection (SOD) particularly challenging in underwater environments.

Recent advances in USOD mainly follow an end-to-end prediction paradigm, typically adopting encoder–decoder architectures to directly map underwater visual observations to binary saliency masks [10]. Benefiting from CNN- and Transformer-based architectures [11], [12], existing methods have achieved encouraging progress [13], [14]. According to the input modality, they can be broadly divided into RGB-based and RGB-D-based methods. RGB-based USOD methods usually extend the visual saliency prediction paradigm of terrestrial SOD to underwater scenes and improve visual saliency inference through underwater image enhancement [15], multi-scale feature fusion [16], and cross-level context aggregation [17]. Since they rely only on underwater RGB images, RGB-based USOD methods are more practical

• Lin Hong, Linan Deng, and Fumin Zhang are with the Department of Electronic and Computer Engineering, The Hong Kong University of Science and Technology, Hong Kong, China.

• Chenhui Wang and Xin Wang are with the School of Robotics and Advanced Manufacture, Harbin Institute of Technology, Shenzhen, China.

• Yuning Cui and Yu Zhang are with the School of Computation, Information and Technology, Technical University of Munich, Munich, Germany.

• Bojian Zhang is with the College of Computer Science & Visual Computing and Intelligent Perception Lab, Nankai University, Tianjin, China.

• Wenqi Ren is with the School of Cyber Science and Technology, Sun Yat-sen University, Shenzhen Campus, Shenzhen, China.

• Xingchen Yang is with the School of Automation, Southeast University, Nanjing, China.

Manuscript received xxx, 2026; revised xxx, 20xx.

for real-world deployment. However, their performance often declines under underwater image degradation. RGB-D-based USOD methods introduce depth information to compensate for degraded visual cues by providing geometric priors and complementary structural information [18], [19]. Although depth cues can improve foreground–background separation in visually ambiguous scenes, reliable and accurate underwater depth information acquisition remains challenging. Consequently, recent RGB-D-based USOD methods often rely on monocular depth estimation [20] or pseudo-depth generation [21], which may introduce unreliable cues and cause error propagation [22]. Moreover, incorporating depth cues into USOD pipelines increases computational overhead and system complexity [23], limiting their practicality for resource-constrained underwater robotic platforms.

To improve visual saliency inference from single RGB images, RGB-based SOD methods have widely exploited structural cues, especially boundary information. Representative works incorporate boundary cues through boundary-aware refinement [24], [25], boundary-guided feature interaction [26], or boundary/interior decoupling [27], [28], improving fine-detail preservation and boundary delineation. More recently, similar ideas have also been introduced into USOD. For example, TC-USOD [21] jointly predicts saliency masks and object boundaries via multi-task learning, while CSUNet [29] uses a dedicated contour refinement module with explicitly supervised fine and coarse contour maps. Nevertheless, existing boundary-aware USOD methods usually treat boundary cues as auxiliary supervision or refinement cues within a unified fixed architecture. Although such a design improves local structural detail modeling, it does not explicitly disentangle boundary-sensitive and region-coherent structural cues.

RGB-based USOD requires the model to distinguish salient objects from degraded underwater scenes using only visual cues, which depends on two complementary structural abilities: precise boundary localization and coherent salient-region formation. The former requires strong sensitivity to local structural discontinuities and thin object structures, whereas the latter relies more on contextual aggregation and region-level structural coherence. These two objectives are complementary but impose different representational demands on feature learning. When boundary localization and region formation are handled through shared intermediate representations and homogeneous decoding procedures, boundary-sensitive and region-oriented features may become entangled and interfere with each other [30]. This issue is further amplified in underwater scenes, where image degradation weakens boundary cues and disrupts regional consistency, leading to fragmented salient regions and blurred boundaries.

In this paper, we characterize this issue as *boundary–region entanglement*, which refers to the insufficient differentiation between boundary-sensitive and region-coherent representational demands in RGB-based USOD. Accordingly, the central challenge of RGB-based USOD is not merely to exploit more structural cues, but to move beyond unified structural modeling toward explicitly differentiated and spatially coordinated boundary-sensitive and region-coherent representations. This observation motivates the proposed **dynamic structural**

**specialization** paradigm. Instead of processing all structural cues within a shared and homogeneous representation, dynamic structural specialization explicitly separates the learning of boundary-sensitive and region-coherent cues, and further coordinates their contributions according to the local structural context. This design is also consistent with studies in visual neuroscience, which suggest that perceptual boundaries and perceptual surfaces are supported by distinct yet interacting mechanisms, while spatial selective attention adaptively biases competing visual cues according to their relevance [31], [32]. **Inspired by this insight, we propose DSS-USOD, a novel RGB-based USOD method built upon dynamic structural specialization**, as shown in Fig. 1. Specifically, DSS-USOD decomposes the extracted shared base representations into a boundary-sensitive branch and a region-coherent branch, which capture fine boundary details and region-level structural consistency, respectively. A spatial coordination module is then introduced to adaptively regulate the relative contributions of the two branches at each spatial location, enabling more reliable object localization, more coherent salient-region formation, and more accurate boundary prediction. Furthermore, a cooperative structural supervision strategy is employed to encourage effective branch specialization and stabilize the spatial coordination between the two branches. The main contributions of this paper are summarized as follows:

- We identify *boundary–region entanglement* as a key challenge in RGB-based USOD, and provide a new perspective that explicitly differentiates and coordinates boundary-sensitive and region-coherent structural representations without relying on auxiliary modalities.
- We propose DSS-USOD, a novel RGB-based USOD framework based on **dynamic structural specialization**, which disentangles boundary-sensitive and region-coherent representations from shared multi-scale features and adaptively coordinates them through a spatial coordination module and cooperative structural supervision.
- Extensive experiments on benchmark datasets and real-world underwater robotic deployment demonstrate the superiority and practical effectiveness of the DSS-USOD.

The rest of this paper is organized as follows: Section II reviews related work. Section III presents the proposed DSS-USOD method. Section IV provides the experimental settings, quantitative and qualitative results, ablation studies, and real-world applications. Finally, Section V concludes this paper.

## II. RELATED WORKS

### A. Underwater Salient Object Detection

Early USOD methods relied on hand-crafted features to identify and segment visually salient objects in underwater scenes [2], [33]. These methods typically exploited low-level cues to distinguish salient objects from background clutter. Although they achieved promising results in relatively simple underwater environments, their performance degraded substantially under severe image degradation, where low-level visual cues become unstable and unreliable. With the rapid development of deep learning algorithms, USOD research has gradually shifted from hand-crafted modeling

to data-driven discriminative learning. Most recent USOD methods adopt encoder–decoder architectures with CNN-based or Transformer-based encoders to learn hierarchical representations [21], [34]. Among them, RGB-based USOD methods have become an increasingly important paradigm due to their practical advantages in real-world underwater deployment. In particular, [35] introduced a physics-inspired multimodal joint learning framework for USOD to alleviate wavelength-dependent color attenuation. In contrast, [36] addressed USOD from the perspective of turbidity–similarity decoupling, where denoising-oriented and similarity-aware subnetworks were jointly optimized through feature-consistent mutual learning. In [37], blurriness-aware representations were explored to enhance robustness under degraded underwater visibility. [29] incorporated boundary-sensitive learning to improve structural perception and boundary localization. [17] leveraged attention-based feature interaction and multi-scale aggregation to strengthen saliency localization, while [38] employed heterogeneous multi-branch interaction to improve complementary feature modeling. Despite their effectiveness, most RGB-based USOD methods still learn saliency cues within a unified representation or rely on fixed feature interactions, limiting their ability to accommodate the spatially varying structural demands of underwater scenes.

Another important line of research introduces depth information as complementary geometric guidance, giving rise to RGB-D-based USOD methods. IF-USOD [18] introduced a multimodal interactive feature enhancement architecture that combines RGB image and depth cues through cross-attention and cross-scale collaborative learning. UDF-Net [19] coupled self-supervised monocular depth estimation with attention-based RGB–depth fusion and task-driven joint optimization to improve underwater visual saliency prediction. [10] further proposed a dual-stage self-paced learning and depth-emphasis strategy to progressively optimize visual saliency inference with enhanced depth-aware guidance. Although these designs can improve foreground–background separation and object localization under severe visual ambiguity, reliable underwater depth information acquisition remains challenging in practice, and large-scale USOD datasets with ground-truth depth remain scarce. Consequently, existing RGB-D-based methods often rely on estimated or pseudo depth cues, which may introduce additional noise and error propagation while increasing computational overhead and system complexity.

### B. Structure-aware Visual Saliency Prediction

Structure-aware modeling has been widely explored in (U)SOD, since accurate visual saliency prediction depend not only on reliable semantic localization but also on the preservation of object boundaries and region completeness. Existing methods generally pursue structural awareness from two aspects: 1) **multi-scale and cross-level interaction**, and 2) **boundary-aware guidance and refinement**. To improve structural awareness through multi-scale fusion and cross-level interaction, PoolNet [39] introduced a global guidance module and a feature aggregation module, in which coarse semantic cues were progressively fused with fine-level features to refine

structural details and improve object localization. MINet [40] further designed aggregate interaction modules to integrate adjacent-level features and self-interaction modules to enhance multi-scale representations, while a consistency-enhanced loss was employed to preserve intra-class consistency in visual saliency prediction. F3Net [41] addressed the structural discrepancy among multi-level features by proposing a cross feature module and a cascaded feedback decoder, enabling complementary features to be iteratively fused and refined for generating saliency maps with clearer local details. These methods improve structural awareness mainly by strengthening feature interaction across scales and levels. Another significant research direction incorporates explicit boundary cues to improve visual saliency inference. EGNet [26] exploited the edge information and region information by progressively fusing saliency features, extracting edge features with both local edge cues and global location cues, and coupling edge features with saliency features at multiple resolutions. BASNet [24] adopted a predict-refine architecture, in which a densely supervised prediction module first estimates a coarse saliency map and a residual refinement module further refines object boundaries; it also introduced a hybrid loss composed of pixel-, patch-, and map-level terms to improve boundary quality. SCRNet [42] modeled the interaction between visual saliency prediction and edge detection by stacking cross-refinement units, where bidirectional message passing was used to jointly refine the multi-level features of the two tasks. These methods demonstrate that boundary cues can effectively reduce boundary ambiguity and improve structural detail preservation. Nevertheless, existing methods usually introduce structural cues through multi-scale fusion or auxiliary boundary guidance within fixed feature processing pipelines. However, these methods rarely explicitly consider the potential boundary–region entanglement, which is essential for fine-grained boundary localization and coherent salient-region perception during visual saliency prediction.

### III. DSS-USOD METHOD

Given an underwater image  $\mathbf{I} \in \mathbb{R}^{3 \times H \times W}$  and its corresponding binary saliency mask  $\mathbf{M} \in \{0, 1\}^{1 \times H \times W}$ , DSS-USOD aims to learn a saliency prediction function:

$$\hat{\mathbf{M}} = \mathcal{F}_{\Theta}(\mathbf{I}), \quad (1)$$

where  $\mathcal{F}_{\Theta}(\cdot)$  denotes DSS-USOD model parameterized by  $\Theta$ , and  $\hat{\mathbf{M}} \in [0, 1]^{1 \times H \times W}$  is the predicted saliency map.

As illustrated in Fig. 2, DSS-USOD adopts an encoder–decoder architecture with dynamic structural specialization as its core. The framework consists of three main components: 1) a shared multi-scale representation learning module extracts and aggregates hierarchical features from the input image; 2) the dynamic structural specialization decomposes the shared representation into two complementary branches, namely a boundary-sensitive (BS) branch and a region-coherent (RC) branch, and uses a spatial coordination module (SCM) to dynamically balance their contributions; and 3) a progressive prediction refinement (PPR) module progressively recovers the saliency map. A cooperative structural supervision strategy is further applied during training to promote branch specialization and stabilize spatial coordination.

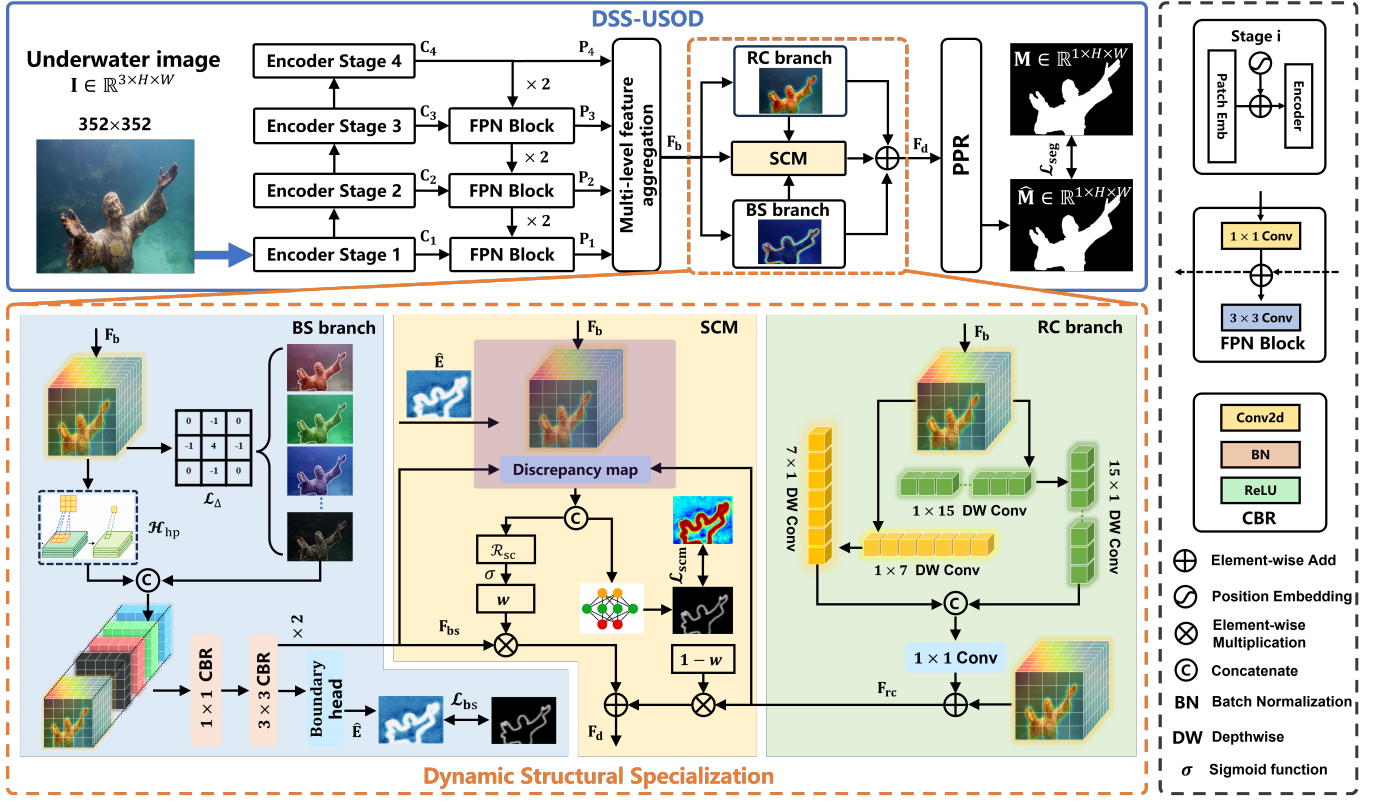


Fig. 2. Overall architecture of the proposed DSS-USOD. Given an underwater RGB image  $\mathbf{I}$ , DSS-USOD extracts hierarchical multi-scale features and aggregates them into a shared base representation  $\mathbf{F}_b$ . Dynamic structural specialization is the core of DSS-USOD, where  $\mathbf{F}_b$  is decomposed into a boundary-sensitive (BS) branch for fine-grained boundary details modeling and a region-coherent (RC) branch for capturing region-level consistency. The spatial coordination module (SCM) dynamically coordinates the BS and RC branches according to local structural context, enabling adaptive balance between boundary precision and region coherence. The saliency map is recovered by progressive prediction refinement (PPR), and cooperative structural supervision is designed to jointly constrain saliency prediction, boundary learning, and spatial coordination during training.

### A. Multi-scale Representation Learning

DSS-USOD employs a hierarchical encoder to extract multi-scale feature maps from the input underwater image:

$$\{\mathbf{C}_1, \mathbf{C}_2, \mathbf{C}_3, \mathbf{C}_4\} = \mathcal{E}(\mathbf{I}), \quad (2)$$

where  $\mathcal{E}(\cdot)$  denotes the encoder, and  $\mathbf{C}_i$  represents the feature map from the  $i$ -th encoder stage.

To facilitate cross-stage aggregation, the feature maps generated at different encoder stages are projected into a unified channel dimension:

$$\tilde{\mathbf{C}}_i = \phi_i(\mathbf{C}_i), \quad i \in \{1, 2, 3, 4\}, \quad (3)$$

where  $\phi_i(\cdot)$  is implemented by a  $1 \times 1$  convolution.

A top-down feature pyramid is then constructed as follows:

$$\mathbf{P}_4 = \tilde{\mathbf{C}}_4, \quad (4)$$

$$\mathbf{P}_3 = \tilde{\mathbf{C}}_3 + \mathcal{U}(\mathbf{P}_4), \quad (5)$$

$$\mathbf{P}_2 = \tilde{\mathbf{C}}_2 + \mathcal{U}(\mathbf{P}_3), \quad (6)$$

$$\mathbf{P}_1 = \tilde{\mathbf{C}}_1 + \mathcal{U}(\mathbf{P}_2), \quad (7)$$

where  $\mathcal{U}(\cdot)$  denotes bilinear upsampling.

To obtain the base representation  $\mathbf{F}_b$ , all pyramid features are resized to the spatial resolution of  $\mathbf{P}_1$  and fused along the channel dimension:

$$\mathbf{F}_b = \Phi_{\text{fuse}}([\mathbf{P}_1, \mathcal{U}_2(\mathbf{P}_2), \mathcal{U}_3(\mathbf{P}_3), \mathcal{U}_4(\mathbf{P}_4)]), \quad (8)$$

where  $[\cdot]$  denotes channel-wise concatenation,  $\mathcal{U}_i(\cdot)$  resizes  $\mathbf{P}_i$  to the resolution of  $\mathbf{P}_1$ , and  $\Phi_{\text{fuse}}(\cdot)$  is implemented by a  $1 \times 1$  convolution followed by GroupNorm and ReLU.

### B. Dynamic Structural Specialization

Given  $\mathbf{F}_b$ , DSS-USOD performs dynamic structural specialization through two coupled operations: 1) decomposing  $\mathbf{F}_b$  into two complementary structural representations, i.e., a boundary-sensitive representation  $\mathbf{F}_{bs}$  and a region-coherent representation  $\mathbf{F}_{rc}$ ; 2) adaptively coordinating the  $\mathbf{F}_{bs}$  and  $\mathbf{F}_{rc}$  according to the local structural context.

1) *Boundary-sensitive (BS) Branch*: The BS branch is designed to capture high-frequency boundary details. In underwater images, object boundaries are often weakened by low contrast and noise, making them difficult to distinguish from the complex background. To enhance boundary-sensitive cues, the BS branch processes the  $\mathbf{F}_b$  through two parallel high-frequency paths: a fixed Laplacian operator and a learnable high-pass transformation, as shown in Fig. 2. The fixed Laplacian path provides an explicit boundary-sensitive inductive bias, while the learnable high-pass path adapts high-frequency enhancement to task-specific boundary patterns. Therefore, the enhanced high-frequency structural response is computed as

$$\mathbf{E}_h = \mathcal{L}_\Delta(\mathbf{F}_b) + \mathcal{H}_{hp}(\mathbf{F}_b), \quad (9)$$

where  $\mathcal{L}_\Delta(\cdot)$  is a fixed channel-wise Laplacian operator and  $\mathcal{H}_{\text{hp}}(\cdot)$  is a learnable high-pass transformation. Specifically,  $\mathcal{H}_{\text{hp}}(\cdot)$  is implemented as a lightweight depthwise  $3 \times 3$  convolution followed by a pointwise  $1 \times 1$  convolution, with batch normalization and ReLU activation.

The  $\mathcal{L}_\Delta(\cdot)$  extracts generic high-frequency responses from each feature channel, thereby highlighting local structural discontinuities around object boundaries. The  $\mathcal{H}_{\text{hp}}(\cdot)$  adapts the boundary enhancement process to task-specific feature patterns, which helps preserve informative boundary cues while reducing noise-sensitive responses. To maintain semantic context during boundary enhancement, the  $\mathbf{F}_b$  and  $\mathbf{E}_h$  are concatenated and transformed as

$$\mathbf{F}_{\text{bs}} = \mathcal{B}([\mathbf{F}_b, \mathbf{E}_h]), \quad (10)$$

where  $\mathcal{B}(\cdot)$  denotes a boundary-sensitive transformation.

The resulting  $\mathbf{F}_{\text{bs}}$  encodes boundary-sensitive structural information for accurate boundary localization. A boundary prediction head is further attached to  $\mathbf{F}_{\text{bs}}$ :

$$\hat{\mathbf{E}} = \sigma(\mathcal{H}_{\text{bs}}(\mathbf{F}_{\text{bs}})), \quad (11)$$

where  $\mathcal{H}_{\text{bs}}(\cdot)$  denotes the boundary prediction head and  $\hat{\mathbf{E}}$  is the predicted boundary probability map.

2) *Region-coherent (RC) Branch*: Boundary-sensitive cues contribute to accurate boundary localization. However, relying solely on high-frequency information may lead to fragmented saliency maps, especially in underwater scenes where object interiors often exhibit low contrast and ambiguous textures. To promote coherent salient-region formation, the RC branch models low-frequency structural consistency by aggregating contextual information over extended spatial ranges. Specifically, we design a residual dual-scale anisotropic large-kernel modeling strategy to capture region-level consistency at different spatial ranges. This strategy is built upon a factorized anisotropic depthwise operator, which serves as the basic building block for large-kernel contextual aggregation. For a kernel size  $k$ , the operator is defined as

$$\mathcal{A}_k(\mathbf{X}) = \delta(\text{BN}(\text{DWConv}_{k \times 1}(\text{DWConv}_{1 \times k}(\mathbf{X})))), \quad (12)$$

where  $\text{DWConv}_{1 \times k}(\cdot)$  and  $\text{DWConv}_{k \times 1}(\cdot)$  denote horizontal and vertical depthwise convolutions, respectively,  $\text{BN}(\cdot)$  is batch normalization, and  $\delta(\cdot)$  is the ReLU activation function. This factorized design approximates a large two-dimensional receptive field with lower computational cost and captures long-range dependencies along different spatial directions.

Based on the operator defined in Eq. (12), the RC branch extracts dual-scale contextual responses and obtains the region-coherent representation through residual enhancement:

$$\mathbf{F}_{\text{rc}} = \mathbf{F}_b + \mathcal{P}_{1 \times 1}(\mathcal{T}_{1 \times 1}([\mathcal{A}_7(\mathbf{F}_b), \mathcal{A}_{15}(\mathbf{F}_b)])), \quad (13)$$

where  $\mathcal{A}_7(\cdot)$  and  $\mathcal{A}_{15}(\cdot)$  denote the factorized anisotropic depthwise contextual operators with kernel sizes of 7 and 15, respectively. They are used to capture region-level contextual dependencies at different spatial ranges.  $\mathcal{T}_{1 \times 1}(\cdot)$  is a pointwise fusion layer that integrates the dual-scale responses, and  $\mathcal{P}_{1 \times 1}(\cdot)$  is a pointwise projection layer that refines the fused representation. The residual connection aims to preserve the

original base representation while incorporating region-level contextual information.

The RC branch emphasizes smooth structural consistency and coherent salient-region activation, which helps suppress isolated noisy responses and reduce fragmented predictions within salient objects, thereby complementing  $\mathbf{F}_{\text{bs}}$  for more reliable underwater visual saliency prediction.

3) *Spatial Coordination Module (SCM)*: The BS and RC branches capture complementary structural properties, i.e., boundary sensitivity and region coherence. However, RGB-based USOD requires structural preferences to vary across spatial locations. Specifically, regions near object boundaries and ambiguous foreground-background transitions rely more on boundary-sensitive high-frequency cues, whereas homogeneous object interiors require region-coherent contextual aggregation to preserve complete salient regions. Therefore, simply fusing the two branches with fixed weights is suboptimal, as it ignores such spatially varying structural demands and the potential entanglement between the BS and RC branches. To address this issue, we design a SCM to adaptively regulate the relative contributions of the BS and RC branches according to the local structural context.

Given  $\mathbf{F}_{\text{bs}}$  and  $\mathbf{F}_{\text{rc}}$ , their structural discrepancy is quantified by explicitly computing the element-wise difference:

$$\mathbf{D} = \frac{1}{C} \sum_{c=1}^C \left| \mathbf{F}_{\text{bs}}^{(c)} - \mathbf{F}_{\text{rc}}^{(c)} \right|, \quad (14)$$

where  $C$  denotes the number of channels, and  $\mathbf{D} \in \mathbb{R}^{1 \times h \times w}$  denotes the branch discrepancy map. A larger value in  $\mathbf{D}$  indicates stronger disagreement between the two specialized representations at the corresponding spatial location.

To estimate the spatial coordination weights, the SCM integrates complementary coordination evidence from the  $\mathbf{F}_b$  and the predicted boundary response  $\hat{\mathbf{E}}$  and  $\mathbf{D}$ :

$$\mathbf{w} = \sigma\left(\mathcal{R}_{\text{sc}}([\mathbf{F}_b, \hat{\mathbf{E}}, \mathbf{D}])\right), \quad (15)$$

where  $\mathcal{R}_{\text{sc}}(\cdot)$  is a lightweight convolutional coordination function implemented by a  $1 \times 1$  convolution, a  $3 \times 3$  convolution, and a final  $1 \times 1$  prediction layer for generating coordination logits. The resulting map  $\mathbf{w} \in [0, 1]^{1 \times h \times w}$  represents the spatial preference for the BS branch, while  $1 - \mathbf{w}$  represents the preference for the RC branch. The dynamically coordinated structural representation is obtained by

$$\mathbf{F}_d = \mathbf{w} \otimes \mathbf{F}_{\text{bs}} + (1 - \mathbf{w}) \otimes \mathbf{F}_{\text{rc}}, \quad (16)$$

where  $\mathbf{F}_d$  denotes coordinated structural representation,  $\otimes$  denotes element-wise multiplication.

Through spatial coordination by the SCM, DSS-USOD can adaptively balance boundary precision and region coherence. The resulting  $\mathbf{F}_d$  integrates both boundary and region cues for generating accurate and complete saliency maps.

### C. Progressive Prediction Refinement

Given the representation  $\mathbf{F}_d$ , the proposed DSS-USOD progressively recovers the full-resolution saliency map in a

coarse-to-fine manner. First, a low-resolution saliency logits map is predicted as

$$\mathbf{S}_s = \mathcal{H}_s(\mathbf{F}_d), \quad (17)$$

where  $\mathcal{H}_s(\cdot)$  denotes a lightweight saliency prediction head, and  $\mathbf{S}_s$  denotes the low-resolution saliency logits.

To construct a coarse full-resolution prediction, DSS-USOD further combines the  $\mathbf{F}_d$  with the  $\mathbf{S}_s$  and feeds them into a learnable coarse prediction head:

$$\mathbf{S}_c = \mathcal{H}_c([\mathbf{F}_d, \mathbf{S}_s]), \quad (18)$$

where  $\mathcal{H}_c(\cdot)$  denotes the coarse prediction head with learnable upsampling, and  $\mathbf{S}_c \in \mathbb{R}^{1 \times H \times W}$  is the coarse full-resolution saliency logits.

Although  $\mathbf{S}_c$  already provides a full-resolution saliency estimate, it may still contain local inaccuracies near object boundaries and ambiguous transition regions. Therefore, DSS-USOD further performs residual refinement by exploiting RGB appearance and shallow spatial features:

$$\mathbf{S}_f = \mathbf{S}_c + \mathcal{H}_r([\mathbf{I}, \mathbf{S}_c, \rho_f(\mathbf{P}_1)]), \quad (19)$$

where  $\rho_f(\cdot)$  denotes channel reduction and full-resolution resizing for  $\mathbf{P}_1$ , and  $\mathcal{H}_r(\cdot)$  is the residual refinement block.

Finally, the saliency probability map is obtained by

$$\hat{\mathbf{M}} = \sigma(\mathbf{S}_f). \quad (20)$$

#### D. Cooperative Structural Supervision

To stabilize the dynamic structural specialization learning, DSS-USOD introduces cooperative structural supervision over saliency prediction, boundary learning, and spatial coordination. Specifically, the decoder generates three saliency logits maps: the final full-resolution logits  $\mathbf{S}_f$ , the coarse full-resolution logits  $\mathbf{S}_c$ , and the low-resolution logits  $\mathbf{S}_s$ .

Let  $\mathbf{M}_s$  denote the ground-truth saliency mask resized to the spatial resolution of  $\mathbf{S}_s$ . The multi-level saliency loss is defined as

$$\begin{aligned} \mathcal{L}_{\text{seg}} = & \lambda_f \mathcal{L}_{\text{str}}(\mathbf{S}_f, \mathbf{M}) + \lambda_c \mathcal{L}_{\text{str}}(\mathbf{S}_c, \mathbf{M}) \\ & + \lambda_s \mathcal{L}_{\text{str}}(\mathbf{S}_s, \mathbf{M}_s), \end{aligned} \quad (21)$$

where  $\mathcal{L}_{\text{str}}(\cdot)$  denotes the structure loss, and  $\lambda_f$ ,  $\lambda_c$ , and  $\lambda_s$  are the weights for final, coarse, and low-resolution supervision, respectively.

To supervise the BS branch, a ground-truth boundary map  $\mathbf{E}$  is first derived from the saliency mask  $\mathbf{M}$  and then resized to the resolution of the predicted boundary logits  $\hat{\mathbf{E}}$ . The boundary loss is formulated as

$$\mathcal{L}_{\text{bs}} = \mathcal{L}_{\text{bce}}^{\text{logit}}(\hat{\mathbf{E}}, \mathbf{E}_s) + \mathcal{L}_{\text{dice}}(\hat{\mathbf{E}}, \mathbf{E}_s), \quad (22)$$

where  $\mathbf{E}_s$  is the resized boundary map,  $\mathcal{L}_{\text{bce}}^{\text{logit}}(\cdot)$  is binary cross-entropy with logits, and  $\mathcal{L}_{\text{dice}}(\cdot)$  is the Dice loss.

To guide spatial coordination between the BS branch and RC branch, a coordination target  $\mathbf{R}_s^*$  is derived from  $\mathbf{E}$ . Specifically, the boundary target is first dilated and then smoothed to highlight boundary and transition regions:

$$\mathbf{R}_s^* = \text{AvgPool}(\text{MaxPool}(\mathbf{E}_s)). \quad (23)$$

The resulting  $\mathbf{R}_s^*$  produces larger responses around object boundaries to emphasize boundary-sensitive cues, while yielding smaller responses within homogeneous object interiors to promote region-coherent cues.

Let  $\mathbf{A}_{\text{sc}}$  denote the spatial coordination logits. The spatial coordination loss is defined as

$$\mathcal{L}_{\text{scm}} = \mathcal{L}_{\text{bce}}^{\text{logit}}(\mathbf{A}_{\text{sc}}, \mathbf{R}_s^*). \quad (24)$$

The **overall training objective** is given by

$$\mathcal{L} = \mathcal{L}_{\text{seg}} + \lambda_{\text{bs}} \mathcal{L}_{\text{bs}} + \lambda_{\text{scm}} \mathcal{L}_{\text{scm}}. \quad (25)$$

where  $\lambda_{\text{bs}}$  and  $\lambda_{\text{scm}}$  are the balancing coefficients for boundary supervision and spatial coordination supervision, respectively.

## IV. EXPERIMENTS

### A. Experimental Setup

1) *Implementation Details*: The proposed DSS-USOD is implemented in PyTorch [43] with pretrained PVTv2 [44] as the encoder backbone. In this paper, two variants are considered: DSS-USOD-T with PVTv2-B3 and DSS-USOD-S with PVTv2-B5, where DSS-USOD-S is used as the default model unless otherwise specified. The model is trained on USOD10K [21], and all input images are resized to  $352 \times 352$  during both model training and inference. DSS-USOD was trained for 50 epochs on an NVIDIA RTX 4090 GPU using the AdamW [45] optimizer, with an initial learning rate of  $1 \times 10^{-4}$ , a weight decay of  $1 \times 10^{-2}$ , and cosine annealing scheduling to a minimum learning rate of  $1 \times 10^{-6}$ . For cooperative structural supervision,  $\mathcal{L}_{\text{str}}$  is applied to the final full-resolution prediction, the coarse full-resolution prediction, and the low-resolution prediction, with weights of 4.0, 0.25, and 0.25, respectively. In addition,  $\mathcal{L}_{\text{bs}}$  and  $\mathcal{L}_{\text{scm}}$  are introduced to stabilize optimization and promote effective branch specialization and adaptive coordination. Mixed-precision training, gradient clipping with a maximum norm of 1.0, and exponential moving average with a decay rate of 0.999 are further adopted to improve the stability and generalization of the final model.

2) *Datasets and Evaluation Metrics*: Quantitative evaluation of the proposed DSS-USOD method are conducted on two widely used benchmark datasets: USOD10K [21] and USOD [46]. Following the common practice, five evaluation metrics are adopted: the S-measure ( $S_m$ ) [47], maximum E-measure ( $E_\xi^{\text{max}}$ ) [48], maximum F-measure ( $\text{max}F$ ) [49], mean absolute error (MAE) [50], and the precision–recall (PR) curve. Specifically,  $S_m$  evaluates the structural similarity between the predicted saliency map and the ground truth from both region-aware and object-aware perspectives.  $E_\xi^{\text{max}}$  measures both local pixel-level matching and global image-level consistency.  $\text{max}F$  computes the harmonic mean of precision and recall over different thresholds, reflecting the overall foreground–background discrimination capability. MAE measures the average absolute difference between the predicted saliency map and the ground-truth mask. The PR curve evaluates the precision–recall trade-off over different thresholds, reflecting the robustness of the predicted saliency maps under varying binarization criteria.

TABLE I

QUANTITATIVE EVALUATION OF THE DSS-USOD BY COMPARING 40 SOTA METHODS. THE PERFORMANCE OF THESE METHODS IS TESTED ON THE USOD10K AND THE USOD DATASETS. THE TOP-3 RESULTS ARE MARKED IN RED, BLUE, AND CYAN, RESPECTIVELY.

Methods	Pub.	USOD10K (1026 images)				USOD (300 images)			
		$S_m \uparrow$	$E_\xi^{\max} \uparrow$	$\max F \uparrow$	MAE $\downarrow$	$S_m \uparrow$	$E_\xi^{\max} \uparrow$	$\max F \uparrow$	MAE $\downarrow$
RGB SOD methods									
BASNet [24]	CVPR_19	.8937	.9378	.8849	.0352	.8941	.9311	.9067	.0490
EGNet [26]	ICCV_19	.9125	.9488	.9040	.0291	.8947	.9278	.9077	.0534
LDf [28]	CVPR_20	.9135	.9574	.9173	.0260	.9027	.9380	.9205	.0447
F3Net [41]	AAAI_20	.9140	.9599	.9171	.0251	.8995	.9355	.9155	.0448
PFPN [51]	AAAI_20	.9090	.9547	.9055	.0302	.8940	.9351	.9077	.0516
MINet [40]	CVPR_20	.9105	.9501	.9072	.0287	.8968	.9329	.9120	.0471
DASNet [52]	ACMMM_20	.9204	.9603	.9212	.0245	.9004	.9350	.9147	.0458
CSNet [58]	TPAMI_22	.8595	.9178	.8462	.0548	.8557	.9051	.8594	.0837
CTDNet [55]	ACMMM_21	.9085	.9531	.9073	.0285	.8924	.9283	.9015	.0476
MFNet [54]	ICCV_21	.8425	.9146	.8193	.0512	.8421	.9105	.8509	.0759
PFSNet [53]	AAAI_21	.8983	.9421	.8966	.0370	.8932	.9281	.9077	.0511
PSGLoss [56]	TIP_21	.8640	.9078	.8508	.0417	.8790	.9262	.9038	.0496
VST [57]	ICCV_21	.9136	.9614	.9108	.0267	.8941	.9322	.9039	.0537
ABiU-Net [60]	TCSVT_24	.9173	.9628	.9192	.0258	.8966	.9343	.9124	.0502
ISNet [59]	TCSVT_24	.9222	.9635	.9203	.0249	.8995	.9352	.9133	.0473
iGAN [61]	TCSVT_25	.9055	.9596	.9033	.0264	.8926	.9372	.9071	.0465
SDNet-A [62]	TPAMI_25	.8882	.9437	.8905	.0340	.8845	.9209	.8928	.0556
RGB-D SOD methods									
JL-DCF [63]	CVPR_20	.9062	.9485	.8978	.0300	.8909	.9292	.9044	.0540
UCNet [64]	CVPR_20	.8997	.9463	.8968	.0301	.8970	.9377	.9158	.0427
S2MA [65]	CVPR_20	.8664	.9208	.8530	.0558	.8627	.9095	.8714	.0791
BBSNet [66]	ECCV_20	.9061	.9512	.9056	.0337	.8855	.9233	.8962	.0596
DANet [67]	ECCV_20	.9006	.9449	.8934	.0279	.8822	.9235	.8987	.0497
DCF [22]	CVPR_21	.9116	.9541	.9045	.0312	.8929	.9307	.9019	.0531
SPNet [68]	ICCV_21	.9075	.9554	.9069	.0280	.8870	.9254	.9019	.0514
HAINet [69]	ICCV_21	.9123	.9552	.9116	.0279	.8957	.9281	.9104	.0494
TriTransNet [70]	ACMMM_21	.7889	.8479	.7501	.0659	.8189	.8844	.8452	.0840
D3Net [71]	TNNLS_21	.8931	.9413	.8807	.0374	.8804	.9211	.8934	.0615
BTS-Net [72]	ICME_21	.9093	.9542	.9104	.0291	.8861	.9206	.8987	.0558
CDINet [73]	ICCV_21	.7049	.8644	.7362	.0904	.6209	.8243	.7208	.1585
CIR-Net [74]	TIP_22	.9109	.9556	.9105	.0307	.8907	.9263	.9030	.0550
PICR-Net [76]	TCSVT_23	.9211	.9640	.9208	.0225	.8956	.9303	.9064	.0460
HiDANet [75]	TIP_23	.9162	.9603	.9175	.0250	.9023	.9393	.9174	.0441
CATNet [77]	TCSVT_24	.9207	.9657	.9237	.0214	.8954	.9291	.9057	.0463
SATNet [78]	TIP_25	.9091	.9559	.9086	.0271	.8900	.9279	.9036	.0497
RGB-D USOD methods									
TC-USOD [21]	TCSVT_23	.9215	.9683	.9236	.0201	.8940	.9332	.9087	.0462
SPDENet [10]	TMM_24	.9233	.9688	.9273	.0199	.9001	.9338	.9134	.0436
FSCDiff [79]	ACMMM_25	.9321	.9712	.9325	.0172	.9058	.9359	.9213	.0404
SearchNet [36]	TIP_26	.9263	.9709	.9288	.0188	.9036	.9465	.9227	.0391
RGB-USOD methods									
SVAM-Net [46]	RSS_22	.7465	.7649	.6451	.0915	.8993	.9409	.9127	.0517
HDANet [35]	TCSVT_25	.9232	.9679	.9266	.0202	.9030	.9377	.9193	.0418
DSS-USOD-T	-	.9325	.9713	.9348	.0194	.9178	.9489	.9278	.0343
DSS-USOD-S	-	.9338	.9740	.9364	.0165	.9222	.9547	.9335	.0299

3) *Compared Methods*: To comprehensively evaluate DSS-USOD, we compare it with 40 representative state-of-the-art (SOTA) methods. The competitor set covers four categories: 17 RGB SOD methods include BASNet [24], EGNet [26], LDf [28], F3Net [41], PFPN [51], MINet [40], DASNet [52], PFSNet [53], MFNet [54], CTDNet [55], PSGLoss [56], VST [57], CSNet [58], ISNet [59], ABiU-Net [60], iGAN [61], and SDNet-A [62]; 17 RGB-D SOD methods include JL-DCF [63], UC-Net [64], S2MA [65], BBS-Net [66], DANet [67], DCF [22], SPNet [68], HAINet [69], TriTransNet [70], D3Net [71], BTS-Net [72], CDINet [73], CIR-Net [74], HiDANet [75], PICR-Net [76], CATNet [77], and SATNet [78]; 2 RGB USOD methods include SVAM-Net [46] and HDANet [35]; 4 RGB-D USOD methods include TC-USOD [21], SPDENet [10], FSCDiff [79], and SearchNet [36]. Such a broad benchmark covers diverse model paradigms, ranging from CNN-based architectures to Transformer-based and diffusion-based designs. In terms of input modality, many methods introduce depth or depth-like cues as auxiliary inputs, whereas DSS-USOD relies solely on a single RGB image. To ensure a fair and consistent comparison, all competing methods are retrained on the USOD10K training set using their official implementations and default training configurations.

### B. Comparison with State-of-the-Art Methods

1) *Quantitative Comparisons*: The proposed DSS-USOD method is quantitatively compared with 40 SOTA methods on

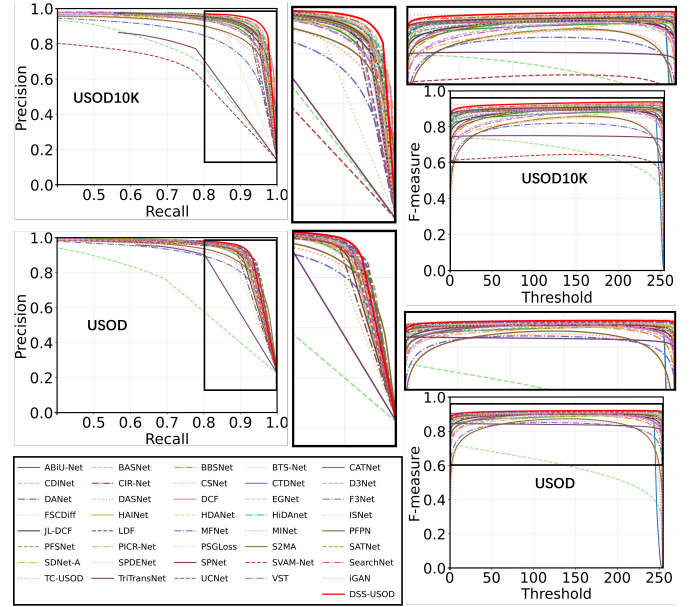


Fig. 3. PR curves and F-measure curves on the USOD10K and USOD.

the USOD10K and USOD datasets under the same evaluation metrics, and the results are shown in Table I.

**Performance on the USOD10K dataset.** On USOD10K, DSS-USOD achieves the best performance across all four evaluation metrics, reaching 0.9338 in  $S_m$ , 0.9740 in  $E_\xi^{\max}$ , 0.9364 in  $\max F$ , and 0.0165 in MAE. Compared with FSCDiff, the strongest competing RGB-D USOD method on this dataset, DSS-USOD improves  $S_m$  by 0.18%,  $E_\xi^{\max}$  by 0.29%, and  $\max F$  by 0.42%, while reducing MAE by 4.07%. These improvements indicate that DSS-USOD not only preserves better structure-aware similarity and foreground separation, but also produces more accurate pixel-level saliency predictions. It is worth noting that DSS-USOD achieves these gains using only RGB input, whereas strong competing methods such as FSCDiff and SearchNet exploit additional depth information. This demonstrates that explicitly modeling boundary-sensitive and region-coherent structural cues can improve RGB-based USOD, while avoiding auxiliary depth cues that would increase computational overhead and system complexity.

**Performance on the USOD dataset.** On the USOD dataset, DSS-USOD also demonstrates strong ability. It achieves the best results across all four evaluation metrics, with 0.9222 in  $S_m$ , 0.9547 in  $E_\xi^{\max}$ , 0.9335 in  $\max F$ , and 0.0299 in MAE. Different from USOD10K, the performance gains on this dataset are more pronounced in terms of prediction error. Compared with SearchNet, the strongest competing RGB-D USOD method in  $E_\xi^{\max}$ ,  $\max F$ , and MAE, DSS-USOD improves  $E_\xi^{\max}$  by 0.87% and  $\max F$  by 1.17%, while reducing MAE by 23.53%. Compared with FSCDiff, DSS-USOD further improves  $S_m$  by 1.81%,  $E_\xi^{\max}$  by 2.01%, and  $\max F$  by 1.32%, while reducing MAE by 25.99%. These results verify the effectiveness of dynamic structural specialization in learning transferable boundary-sensitive and region-coherent cues for underwater visual saliency inference.

Fig. 3 compares the PR curves and F-measure curves

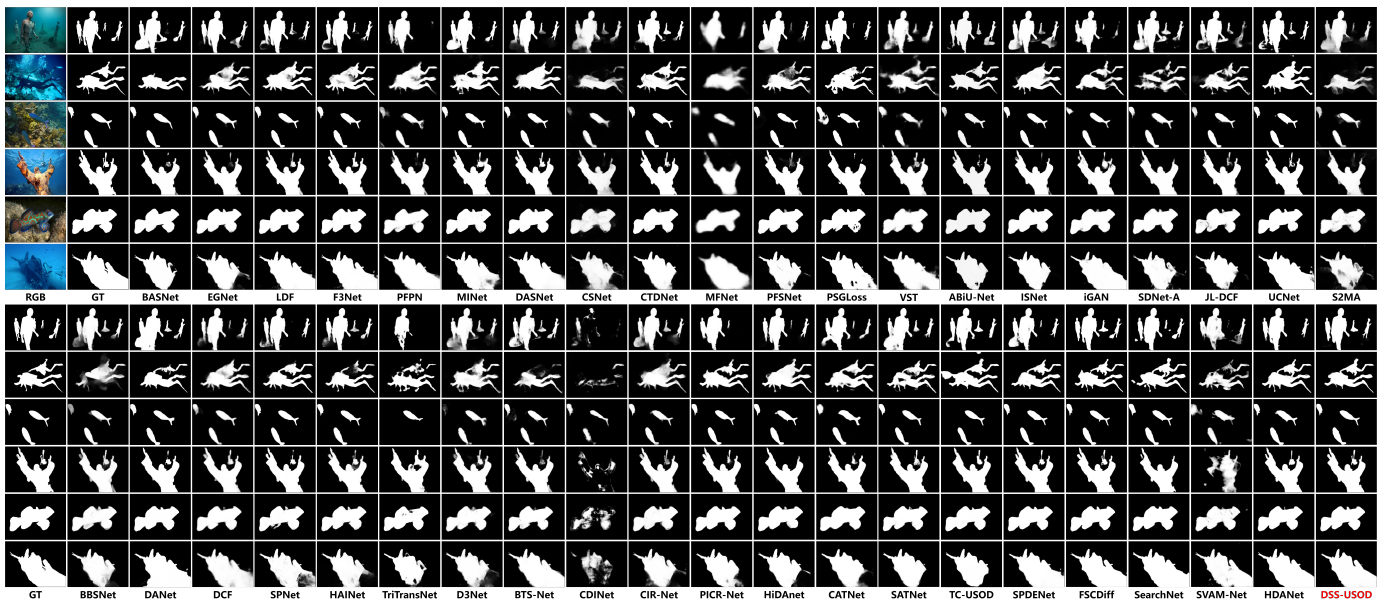


Fig. 4. Qualitative visual comparison of DSS-USOD with 40 SOTA methods on USOD10K (first three rows) and USOD (last three rows). Owing to its dynamic structural specialization, DSS-USOD better preserves fine object boundaries while maintaining regional coherence, leading to more accurate visual saliency inference in challenging underwater scenes, zoom-in for more details. (GT: ground-truth map).

of different methods on USOD10K and USOD. Overall, DSS-USOD maintains competitive precision–recall behavior on both benchmark datasets, indicating its ability to distinguish salient objects from degraded underwater scenes. On USOD10K, DSS-USOD achieves consistently high precision across a wide range of recall values and obtains a superior F-measure curve, which is consistent with its leading  $\max F$  score in Table I. On USOD, DSS-USOD also remains among the top-performing methods across different thresholds, further showing its stability under cross-dataset evaluation. These curve-based comparisons are consistent with the quantitative results, further demonstrating the effectiveness and superior performance of the proposed DSS-USOD method.

To further analyze the influence of encoder backbone, we evaluate DSS-USOD with different CNN- and Transformer-based backbones, as shown in Table II. In general, stronger backbones lead to better performance, indicating the importance of high-quality hierarchical representations for RGB-based USOD. Among CNN-based backbones, ConvNeXt variants consistently outperform ResNet variants, demonstrating the advantage of modern convolutional architectures. Among Transformer-based backbones, PVTv2 achieves strong overall performance, especially on USOD10K. Specifically, DSS-USOD-S with PVTv2-B5 achieves the best results across all four metrics on USOD10K, while DSS-USOD-T with PVTv2-B3 provides competitive performance with fewer parameters. These results show that DSS-USOD is compatible with different backbones, and stronger hierarchical feature extractors can further enhance visual saliency prediction performance.

Overall, DSS-USOD achieves the best overall results on the two benchmark datasets, confirming the effectiveness of the proposed method. Notably, DSS-USOD surpasses RGB-D-based SOD/USOD methods while using only RGB input,

demonstrating that explicitly modeling boundary-sensitive and region-coherent structural cues can deliver strong RGB-based USOD performance without auxiliary depth cues.

2) *Qualitative Comparisons*: Fig. 4 presents the qualitative comparison between DSS-USOD and 40 SOTA methods. Consistent with the quantitative results in Table I, generic RGB SOD methods show limited robustness when directly applied to underwater scenes. Although BASNet and EGNet incorporate boundary-related cues, they are developed for terrestrial SOD and still suffer from incomplete regions, blurred contours, or background distractions under underwater image degradation. Other RGB SOD methods can roughly localize salient objects in some cases, but they often lack stable boundary delineation and region completeness in challenging underwater scenes. RGB-D SOD methods generally improve object localization by exploiting depth-related cues. However, since they are mainly designed for terrestrial RGB-D SOD, their predictions may still contain background noise, miss fine structures, or generate coarse boundaries when transferred to underwater scenes. USOD-specific methods, such as FSCDiff, SearchNet, and HDANet, show stronger adaptation to underwater environments, but they may still produce fragmented salient regions, coarse contours, or false positives in complex backgrounds. In contrast, DSS-USOD produces more coherent salient regions and more accurate object contours across diverse underwater scenes. It better preserves small or slender structures and suppresses distracting background responses under severe degradation. These qualitative results further demonstrate that dynamic structural specialization enables DSS-USOD to effectively balance boundary precision and region coherence for robust RGB-based USOD.

3) *Complexity-Performance Trade-off Analysis*: To evaluate the deployment potential of DSS-USOD, we analyze the trade-off between model complexity and USOD performance. Here,

TABLE II  
PERFORMANCE AND PARAMETER COMPARISON OF DSS-USOD WITH  
DIFFERENT BACKBONES ON USOD10K AND USOD DATASETS.

Backbone	Params	USOD10K (1026 images)				USOD (300 images)			
		$S_m \uparrow$	$E_{\xi}^{\max} \uparrow$	$\max F \uparrow$	MAE $\downarrow$	$S_m \uparrow$	$E_{\xi}^{\max} \uparrow$	$\max F \uparrow$	MAE $\downarrow$
ResNet-50 [80]	29.16M	.9164	.9609	.9173	.0255	.8995	.9363	.9073	.0427
ResNet-101 [80]	48.15M	.9221	.9644	.9243	.0235	.9014	.9400	.9143	.0418
ConvNeXt-Tiny [81]	32.86M	.9287	.9685	.9308	.0199	.9127	.9448	.9243	.0364
ConvNeXt-Small [81]	54.49M	.9319	.9707	.9341	.0185	.9174	.9487	.9280	.0338
ConvNeXt-Base [81]	92.60M	.9309	.9712	.9341	.0191	.9187	.9514	.9313	.0327
Swin-Tiny [82]	32.83M	.9261	.9661	.9267	.0218	.9132	.9451	.9226	.0350
Swin-Small [82]	54.13M	.9282	.9679	.9286	.0207	.9240	.9572	.9345	.0304
PVTv2-B1 [44]	17.52M	.9259	.9664	.9272	.0224	.9120	.9458	.9238	.0370
PVTv2-B3 [44]	49.62M	.9325	.9713	.9348	.0194	.9178	.9489	.9278	.0343
PVTv2-B5 [44]	86.42M	.9338	.9740	.9364	.0165	.9222	.9547	.9335	.0299

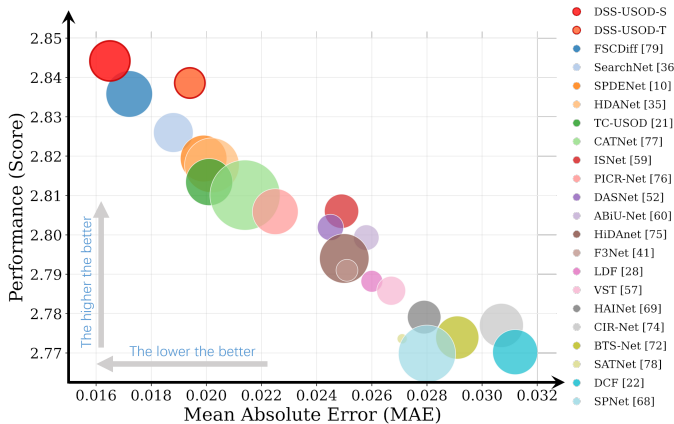


Fig. 5. Trade-off between model complexity and performance. The horizontal axis denotes MAE, and the vertical axis is the sum of three positive-oriented metrics, including  $S_m$ ,  $E_{\xi}^{\max}$ , and  $\max F$ . The circle size represents model size. Methods closer to the upper-left region with smaller circles indicate a better trade-off between model complexity and performance.

model complexity is measured by the number of model parameters. Specifically, we compare DSS-USOD with the top 20 representative methods selected according to their overall performance on USOD10K, in terms of parameter size and quantitative performance, as shown in Fig. 5. In the visualization, MAE is used as the horizontal axis, while the sum of three positive-oriented metrics, including  $S_m$ ,  $E_{\xi}^{\max}$ , and  $\max F$ , is used as the vertical axis. The circle size represents the number of model parameters. Therefore, methods closer to the upper-left region with smaller circles indicate a better trade-off between USOD performance and model complexity. Compared with RGB-D-based USOD methods, DSS-USOD does not rely on depth information, thereby avoiding the additional cost introduced by depth sensing and modality-specific processing. Compared with existing RGB-based USOD methods, DSS-USOD maintains a favorable complexity–performance trade-off through its lightweight dynamic structural specialization design. Overall, DSS-USOD achieves strong performance with a reasonable parameter size, demonstrating its practicality for deployment on underwater robotic platforms.

### C. Generalization to Terrestrial Environments

Although DSS-USOD is designed for underwater environments, its core design addresses the general boundary–region entanglement problem in visual saliency prediction,

which may also benefit generic SOD. To evaluate its cross-domain generalization ability, we directly test DSS-USOD-S on six widely used RGB SOD benchmarks without additional fine-tuning, including DUTS-TE [101], DUT-OMRON [102], HKU-IS [103], ECSSD [104], SOD [105], and PASCAL-S [106]. DSS-USOD is compared with 30 representative SOTA SOD methods, and the quantitative results are shown in Table III. As shown in Table III, DSS-USOD achieves competitive cross-domain performance on terrestrial SOD benchmarks, despite being trained for underwater scenes. In particular, DSS-USOD shows strong and stable performance in terms of MAE. It achieves the best MAE on HKU-IS and PASCAL-S, the second-best MAE on DUTS-TE and ECSSD, and the third-best MAE on SOD. On DUT-OMRON, DSS-USOD obtains an MAE of 0.044, which is also close to the top-performing methods. These results indicate that the learned structural representation can still produce low-error saliency map predictions under a clear domain shift from underwater to terrestrial scenes. For structure-aware evaluation, DSS-USOD also remains competitive. It obtains top-three  $S_m$  results on DUTS-TE, ECSSD, HKU-IS, and PASCAL-S, suggesting that the proposed boundary-sensitive and region-coherent modeling captures transferable structural cues. However, DSS-USOD does not consistently achieve top performance in  $\max F$ , especially on DUT-OMRON and SOD. This is reasonable because  $\max F$  is more sensitive to threshold-dependent foreground separation, while the compared SOD methods are specifically designed and trained for terrestrial benchmarks. Overall, the generalization results suggest that DSS-USOD does not merely exploit underwater-specific appearance patterns. Instead, dynamic structural specialization learns transferable boundary–region cues that remain effective for generic SOD, especially in reducing pixel-level prediction errors. The remaining gap on some threshold-dependent metrics also indicates that incorporating terrestrial data or domain adaptation could further improve its universal saliency prediction capability.

### D. Ablation Study

To validate the effectiveness of dynamic structural specialization in DSS-USOD, we conduct comprehensive ablation studies on its key components and design choices. These studies are designed to examine whether explicitly disentangling boundary-sensitive and region-coherent cues, spatially coordinating their contributions, and supervising their specialization can improve RGB-based USOD. In particular, we aim to answer the following four questions:

- (1) Whether explicitly disentangling boundary-sensitive and region-coherent representations benefits RGB-based USOD?
- (2) Whether the SCM is necessary for modeling spatially varying structural preferences?
- (3) Whether the cooperative structural supervision improves branch specialization and spatial coordination during training?
- (4) Whether the PPR strategy contributes to final prediction?

1) *Effectiveness of the two-branch Structural Specialization:* **To answer the question (1)**, we construct several DSS-USOD variants by progressively introducing the BS and RC branches to evaluate the effectiveness of the proposed two-branch structural specialization. The baseline model predicts

TABLE III

GENERALIZATION EVALUATION RESULTS OF DSS-USOD ON RGB SOD DATASETS: DUTS, DUT-OMRON, HKU-IS, ECSSD, SOD, AND PASCAL-S. THE TOP THREE RESULTS ARE HIGHLIGHTED IN RED, BLUE, AND CYAN, RESPECTIVELY. “-” INDICATES THAT THE CORRESPONDING RESULT WAS NOT REPORTED IN THE ORIGINAL WORK.

Methods	Pub.	DUTS-TE			ECSSD			DUT-OMRON			HKU-IS			SOD			PASCAL-S		
		$S_m \uparrow$	$\max F \uparrow$	MAE $\downarrow$	$S_m \uparrow$	$\max F \uparrow$	MAE $\downarrow$	$S_m \uparrow$	$\max F \uparrow$	MAE $\downarrow$	$S_m \uparrow$	$\max F \uparrow$	MAE $\downarrow$	$S_m \uparrow$	$\max F \uparrow$	MAE $\downarrow$	$S_m \uparrow$	$\max F \uparrow$	MAE $\downarrow$
FC-SOD [83]	NeurIPS <sub>20</sub>	-	.846	.045	-	-	-	-	.767	.067	-	-	-	-	.846	.122	-	.848	.067
LDF [28]	CVPR <sub>20</sub>	-	-	.034	-	-	.034	-	.051	-	-	.027	-	-	-	-	-	-	.060
MINet [40]	CVPR <sub>20</sub>	.884	.884	.037	.925	.947	.033	.833	.810	.055	.920	.935	.028	-	-	-	.857	.882	.064
F3Net [41]	AAAI <sub>20</sub>	.888	-	.035	.924	-	.033	.838	-	.053	.917	-	.028	-	-	-	.855	-	.062
PFPN [51]	AAAI <sub>20</sub>	.887	.888	.037	.932	.949	.033	.842	.820	.053	.921	.939	.030	-	-	-	.851	.892	.068
HVPNet [84]	TCYB <sub>20</sub>	-	-	.058	-	-	.055	-	-	.064	-	-	.045	-	-	.122	-	-	
CTDNet [55]	ACM MM <sub>21</sub>	-	-	.034	-	-	.032	-	-	.052	-	-	.027	-	-	-	-	.061	
MFNet [54]	ICCV <sub>21</sub>	.775	-	.076	.834	-	.084	.742	-	.087	.846	-	.059	-	-	.770	-	.115	
PFSNet [53]	AAAI <sub>21</sub>	-	.898	.036	-	.952	.031	-	.823	.055	-	.943	.026	-	-	-	.881	.063	
SGL-KRN [85]	AAAI <sub>21</sub>	-	.898	.034	-	.946	.036	-	.827	.049	-	.939	.028	-	-	-	.872	.067	
PSGLoss [56]	TIP <sub>21</sub>	-	.890	.036	-	.946	.035	-	.828	.053	-	.938	.027	-	.872	.096	-	.879	.061
SAMNet [86]	TIP <sub>21</sub>	-	.835	.058	-	.925	.053	-	.797	.065	-	.915	.045	-	.833	.123	-	-	
DPNet [87]	TIP <sub>22</sub>	.912	-	.029	.937	-	.028	.853	-	.049	.934	-	.023	-	-	.856	-	.072	
EDN-R [88]	TIP <sub>22</sub>	.892	.893	.035	.927	.950	.033	.849	.821	.050	.924	.940	.027	-	-	.865	.879	.062	
CSNet [58]	TPAMI <sub>22</sub>	-	.819	.074	-	.916	.066	-	.792	.080	-	.899	.059	-	.825	.137	-	.835	.102
TSPORTNet [89]	TPAMI <sub>22</sub>	.871	-	.043	.913	-	.041	.823	-	.058	.909	-	.032	-	-	.850	-	.071	
DCENet [90]	TCSVT <sub>22</sub>	-	.889	.038	-	.948	.035	-	.837	.055	-	.935	.030	-	.883	.089	-	.885	.062
DHNet [91]	TCSVT <sub>22</sub>	.897	.886	.033	.931	.945	.031	.850	.799	.052	.924	.935	.026	-	-	.870	.867	.059	
MEENet [92]	CVPR <sub>23</sub>	.905	.912	.028	.928	.955	.031	.850	.834	.045	.927	.948	.023	.809	.878	.087	.872	.890	.054
BBRF [93]	TIP <sub>23</sub>	.908	.916	.025	.939	.963	.022	.855	.843	.042	.935	.958	.020	-	-	.871	.891	.049	
ICON-S [94]	TPAMI <sub>23</sub>	.917	-	.025	.941	-	.023	.869	-	.043	.935	-	.022	.825	-	.083	-	.885	.048
PRNet-R [95]	TMM <sub>23</sub>	.897	.881	.039	.917	.939	.039	.829	.804	.056	.913	.931	.032	-	-	.853	.877	.067	
VSCode-S [96]	CVPR <sub>24</sub>	.926	.922	-	.949	.959	-	.877	.840	-	.940	.951	-	.870	.882	-	.887	.864	
VST-S++ [97]	TPAMI <sub>24</sub>	.909	.897	.029	.939	.951	.027	.859	.813	.050	.932	.941	.025	.859	.866	.059	.880	.859	.062
ELSANet [98]	TCSVT <sub>24</sub>	-	.882	.034	-	.943	.030	-	.794	.050	-	.935	.025	-	-	-	-	.862	.059
ABUINet [60]	TCSVT <sub>24</sub>	.904	.906	.029	.936	.959	.026	.860	.843	.043	.932	.951	.021	.797	.879	.089	-	-	
SENet [99]	TIP <sub>25</sub>	.926	.925	.022	.949	.964	.020	.876	.835	.040	.941	.953	.019	-	-	.890	.886	.046	
SDNet [62]	TPAMI <sub>25</sub>	.839	.816	.057	.908	.922	.045	.818	.773	.067	.903	.915	.038	.788	.798	.113	.820	.815	.089
iGAN [61]	TCSVT <sub>25</sub>	.912	-	.026	.941	-	.025	.861	-	.047	.929	-	.023	.861	-	.060	-	.879	.053
SAMBA [100]	CVPR <sub>25</sub>	.932	.930	-	.953	.965	-	.889	.859	-	.945	.956	-	-	-	.892	.896	-	
DSS-USOD	-	.922	.916	.023	.944	.957	.021	.873	.837	.044	.940	.950	.018	.826	.860	.082	.887	.889	.046

saliency maps from  $F_b$  without explicit structural specialization. The “+BS” and “+RC” variants introduce only the BS branch and the RC branch, respectively, while the full DSS-USOD incorporates both branches. As shown in Table IV, introducing the RC branch improves the baseline by increasing  $S_m$  by 0.41% and reducing MAE by 1.60%. This indicates that region-coherent modeling helps maintain complete salient regions in degraded underwater scenes. In contrast, using the BS branch alone leads to inferior performance, suggesting that boundary-sensitive cues may be unstable without sufficient region-level contextual support. When both branches are incorporated, DSS-USOD achieves the best performance across all metrics. Compared with the baseline, DSS-USOD improves  $S_m$  by 1.03% and  $\max F$  by 1.33%, while reducing MAE by 12.23%. These results demonstrate that the BS and RC branches provide complementary structural cues and jointly improve the balance between boundary precision and region completeness. Fig. 6 further visualizes the training evolution of the two branches. As training proceeds, the BS branch gradually focuses on object boundaries, while the RC branch progressively captures more coherent salient regions. The final prediction also becomes increasingly accurate, further supporting the complementarity between boundary-sensitive and region-coherent structural learning.

To further illustrate how DSS-USOD differs from existing boundary-aware methods in addressing *boundary–region entanglement*, we visualize the training evolution of boundary and region representations for four boundary-aware methods in Fig. 7. For BASNet [24], the boundary predictions are clean, but the model fails to accurately localize the salient object, leading to incomplete saliency masks. EGNet [26] achieves more accurate target localization, but its boundary predictions are less precise, resulting in coarse saliency edges in the

TABLE IV

ABLATION STUDY OF STRUCTURAL SPECIALIZATION ON USOD10K. “BS” AND “RC” DENOTE THE BOUNDARY-SENSITIVE BRANCH AND THE REGION-COHERENT BRANCH.

Variant	BS	RC	$S_m \uparrow$	$E_{\xi}^{\max} \uparrow$	$\max F \uparrow$	MAE $\downarrow$
Baseline	-	-	.9243	.9709	.9241	.0188
+ BS	✓	-	.9265	.9657	.9256	.0183
+ RC	-	✓	.9281	.9700	.9319	.0185
DSS-USOD	✓	✓	<b>.9338</b>	<b>.9740</b>	<b>.9364</b>	<b>.0165</b>

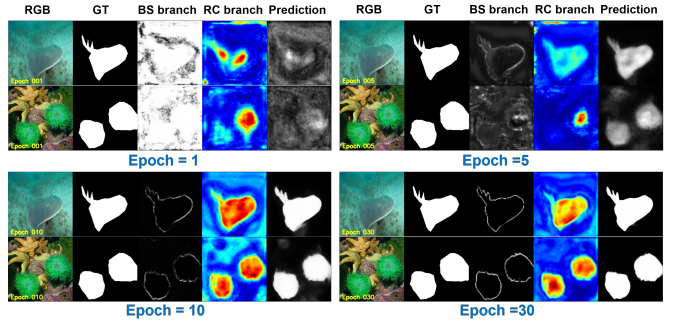


Fig. 6. Visualization of the training evolution of the two specialized branches. As training proceeds, the BS branch gradually learns to emphasize boundaries, while the RC branch progressively captures coherent salient regions, leading to increasingly accurate saliency predictions.

final output. TC-USOD [21] improves upon EGNet with more accurate boundary predictions, yet still incorrectly segments some background regions. In contrast, DSS-USOD produces both clean and accurate boundary predictions and correctly localizes the salient object. Moreover, the visualization of the BS branch weight map ( $w$ ) demonstrates the effectiveness of the proposed dynamic structural specialization in adap-

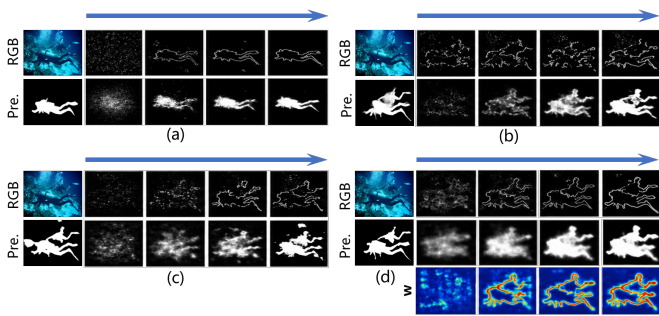


Fig. 7. Training progression of boundary and region representations across four methods: (a) BASNet [24], (b) EGNNet [26], (c) TC-USOD [21], and (d) DSS-USOD. The first column shows the input image (top) and final saliency prediction (bottom), the subsequent columns display intermediate boundary and region feature maps over training. DSS-USOD additionally shows weight map ( $w$ ) of BS branch, illustrating the effectiveness of the designed SCM.

TABLE V

ABLATION STUDY OF THE DESIGNED BRANCH COORDINATION STRATEGY.

Coordination strategy	$S_m \uparrow$	$E_\xi^{\max} \uparrow$	$\max F \uparrow$	MAE $\downarrow$
Fixed averaging	.9318	.9724	.9342	.0179
Global scalar weighting	.9321	.9717	.9335	.0173
Concatenation + Conv	.7125	.7297	.7162	.0510
SCM	<b>.9338</b>	<b>.9740</b>	<b>.9364</b>	<b>.0165</b>

tively balancing boundary-sensitive and region-coherent cues across spatial locations. Consequently, while previous methods improve structural details to some extent, only DSS-USOD explicitly disentangles boundary and region representations and resolves their potential representational conflict, leading to more accurate and coherent saliency predictions.

2) *Effectiveness of the SCM*: **To answer the question (2)**, we compare SCM with several alternative branch coordination strategies, including fixed averaging, learnable global scalar weighting, and concatenation followed by convolution. Since the BS and RC branches encode complementary structural representations, fixed or globally shared fusion weights are insufficient for underwater scenes, where object boundaries, salient interiors, and ambiguous degraded regions require different structural cues. The quantitative results are shown in Table V. Fixed averaging and global scalar weighting achieve competitive performance, but they are still inferior to SCM, indicating that spatially adaptive coordination provides additional benefits over static or globally learned fusion rules. In contrast, concatenation followed by convolution causes a clear performance drop. Although this strategy introduces learnable fusion, it directly mixes the two specialized representations without explicitly modeling their spatial preference, which may weaken the complementarity between boundary-sensitive and region-coherent cues. The visualization comparisons in Fig. 8 support these findings. For simple scenes with clear foreground-background separation, fixed averaging, global scalar weighting, and SCM produce similar saliency maps, consistent with their close quantitative results. In complex scenes with weak boundaries, cluttered backgrounds, or thin structures, SCM shows clearer advantages by preserving fine details and suppressing ambiguous background responses.

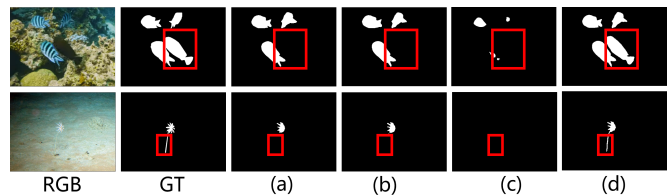


Fig. 8. Qualitative comparison of different branch coordination strategies in the proposed DSS-USOD method. (a) Fixed averaging. (b) Global scalar weighting. (c) Concatenation + Conv. (d) SCM.

TABLE VI

ABLATION STUDY OF COOPERATIVE STRUCTURAL SUPERVISION. “BND.” AND “COORD.” DENOTE BOUNDARY SUPERVISION AND COORDINATION SUPERVISION, RESPECTIVELY.

Supervisions	Bnd.	Coord.	$S_m \uparrow$	$E_\xi^{\max} \uparrow$	$\max F \uparrow$	MAE $\downarrow$
w/o both	-	-	.9311	.9719	.9323	.0171
w/o Bnd.	-	✓	.9304	.9718	.9333	.0190
w/o Coord.	✓	-	.9297	.9707	.9315	.0185
Full model	✓	✓	<b>.9338</b>	<b>.9740</b>	<b>.9364</b>	<b>.0165</b>

By contrast, concatenation followed by convolution performs poorly in both simple and complex scenes, often yielding incomplete regions and inaccurate boundaries. These results confirm the importance of SCM in the proposed DSS-USOD.

3) *Effectiveness of the Cooperative Structural Supervision*: **To answer the question (3)**, we construct several DSS-USOD variants by removing boundary supervision, coordination supervision, or both, to analyze the effectiveness of the proposed cooperative structural supervision. The results are summarized in Table VI. The full model with both supervision terms achieves the best performance across all evaluation metrics, demonstrating the effectiveness of cooperative structural supervision. Compared with the variant without auxiliary supervision, the full model improves  $S_m$  from 0.9311 to 0.9338 and  $\max F$  from 0.9323 to 0.9364, while reducing MAE from 0.0171 to 0.0165. Using only one type of auxiliary structural supervision brings limited improvement, indicating that boundary supervision and coordination supervision are complementary. Their combination promotes more effective branch specialization and more stable adaptive coordination. The qualitative results in Fig. 9 further support these findings. For simple scenes, all variants can roughly detect the salient objects, while DSS-USOD preserves more complete structures and finer details. For complex scenes, the variants without complete cooperative supervision often fail to accurately localize salient objects or produce unreliable predictions, whereas DSS-USOD generates clearer and more accurate saliency maps with fewer distractions. These results demonstrate that cooperative structural supervision plays a crucial role in enabling effective dynamic structural specialization in DSS-USOD.

4) *Effectiveness of the PPR Strategy*: **To answer question (4)**, we compare DSS-USOD with two decoder-related variants: 1) DSS-USOD-v1, which uses only the low-resolution prediction; and 2) DSS-USOD-v2, which further adds the coarse full-resolution decoder. For DSS-USOD-v1, the low-resolution prediction is bilinearly upsampled to the input res-

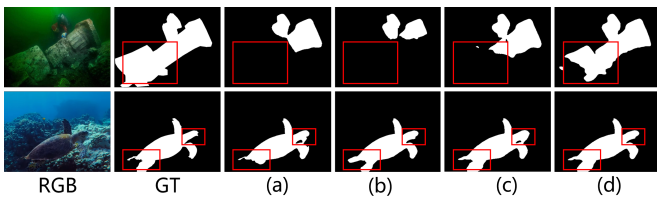


Fig. 9. Qualitative comparison of different supervision strategies in the proposed DSS-USOD method. (a) without both boundary supervision and coordination supervision. (b) without boundary supervision. (c) without coordination supervision. (d) with full cooperative structural supervision.

TABLE VII  
ABLATION STUDY OF THE PPR STRATEGY. “LOW-RES”, “COARSE”, AND “REFINE” DENOTE THE LOW-RESOLUTION PREDICTION, THE COARSE FULL-RESOLUTION DECODER, AND THE FINAL REFINEMENT MODULE, RESPECTIVELY.

Methods	Low-res	Coarse	Refine	$S_m \uparrow$	$E_\xi^{\max} \uparrow$	$\max F \uparrow$	MAE $\downarrow$
DSS-USOD-v1	✓	-	-	.5659	.5669	.5056	.1220
DSS-USOD-v2	✓	✓	-	.9299	.9717	.9324	.0182
DSS-USOD	✓	✓	✓	<b>.9338</b>	<b>.9740</b>	<b>.9364</b>	<b>.0165</b>

olution, while DSS-USOD-v2 uses the coarse full-resolution prediction as the final output. The results are shown in Table VII. Directly using the upsampled low-resolution prediction leads to poor performance, with  $S_m$  of 0.5659 and MAE of 0.1220. Introducing the coarse full-resolution decoder substantially improves the results, increasing  $S_m$  to 0.9299 and reducing MAE to 0.0182. With the final refinement module, DSS-USOD further improves all metrics, achieving 0.9338 in  $S_m$ , 0.9740 in  $E_\xi^{\max}$ , 0.9364 in  $\max F$ , and 0.0165 in MAE. These results show that PPR progressively improves full-resolution visual saliency prediction. The visualization in Fig. 10 further supports the ablation results. DSS-USOD-v1 can roughly localize salient objects but fails to generate complete masks or clear boundaries. DSS-USOD-v2 produces more complete salient regions, but its predictions may still include background responses. In contrast, the DSS-USOD with PPR strategy can generate cleaner saliency maps with better boundary delineation and fewer background false positives. Overall, these results demonstrate that the PPR strategy effectively transfers the structural advantages of the coordinated representation to the final visual saliency prediction.

### E. Real-world Application

To evaluate the practical applicability of the proposed DSS-USOD method, we deploy the trained DSS-USOD-T model on an underwater robot and test it in a real-world underwater object inspection task. As shown in Fig. 11, the underwater robot is equipped with RGB cameras and an onboard embedded computing unit. The onboard perception system is built on an NVIDIA Jetson TX2 NX module, where the captured RGB images are processed locally without relying on an external workstation. During deployment, the input images are resized to  $352 \times 352$ , consistent with the training and testing settings. DSS-USOD-T runs in a fully feed-forward manner and directly outputs saliency maps from single underwater RGB images. Fig. 12(a) shows an overview

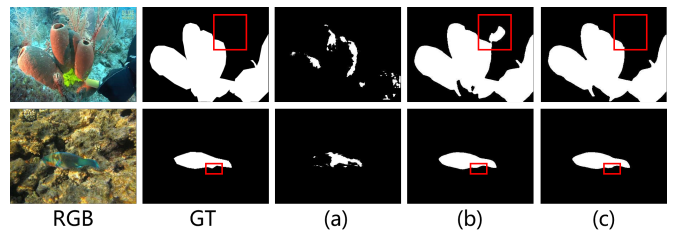


Fig. 10. Qualitative comparison of different PPR variants. From left to right: input image, ground truth, (a) DSS-USOD-v1 prediction, (b) DSS-USOD-v2 prediction, and (c) DSS-USOD prediction.

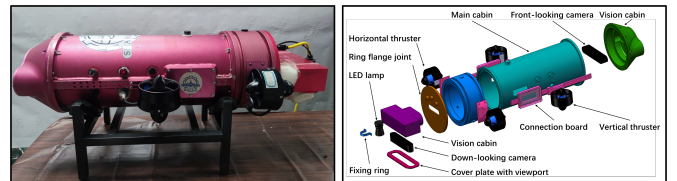


Fig. 11. Underwater robots used for practical application of DSS-USOD.

of the experimental environment, including the water tank setup, target object, and underwater robot. During deployment, DSS-USOD-T does not require additional sensing modalities, iterative optimization, or task-specific post-processing. This design enables stable onboard inference and makes the model suitable for resource-constrained underwater robotic systems. In the underwater object inspection task, the DSS-USOD-T achieves an average inference speed of 21 FPS on the Jetson TX2 NX, demonstrating its capability for real-time onboard visual perception. In this experiment, the underwater robot performs close-range visual observation of objects in the water tank and continuously captures RGB images under underwater conditions. The predicted saliency maps highlight visually distinctive foreground targets while suppressing distracting background regions and water-induced noise. As a result, the robot obtains clear target localization and reliable structural perception, which can support subsequent inspection-related operations such as region-of-interest identification, object-centered observation, and visual analysis. Qualitative examples of visual saliency prediction during the underwater object inspection task are shown in Fig. 12(b) and Fig. 12(c). These real-world experiments demonstrate that DSS-USOD not only achieves strong performance on benchmark datasets but also shows practical applicability to underwater robotic systems for vision-guided underwater tasks. The video is available at: <https://github.com/LinHong-HIT/DSS-USOD>.

## V. CONCLUSION

In this paper, we presented DSS-USOD, a novel RGB-based USOD method that robustly generates accurate saliency maps from single underwater images without relying on auxiliary depth modality. Motivated by the observation that reliable USOD requires spatially varying structural preferences, DSS-USOD addresses the issue of boundary–region entanglement through dynamic structural specialization. Specifically, DSS-USOD first constructs a shared base representation from the

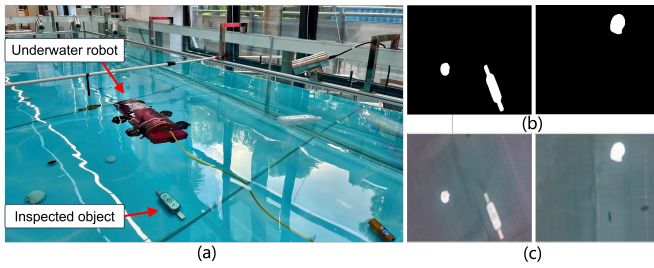


Fig. 12. Underwater robotic visual target inspection. (a) Experimental setup. (b) Camera view of the target object. (c) Visual saliency inference result generated by the proposed DSS-USOD.

input underwater image, then decomposes it into boundary-sensitive and region-coherent representations, and further adaptively coordinates their contributions through a spatial coordination module. In addition, a cooperative structural supervision strategy is introduced to promote effective branch specialization and stable spatial coordination. Extensive experiments on benchmark datasets demonstrate that DSS-USOD outperforms existing SOTA methods. Comprehensive ablation studies further verify the effectiveness of the proposed structural specialization, spatial coordination, cooperative supervision, and progressive prediction refinement designs. Moreover, real-world deployment on an underwater robot validates the practical value of DSS-USOD in vision-guided underwater tasks. We hope this work offers a new perspective on RGB-based USOD by demonstrating the importance of explicitly disentangling and dynamically coordinating complementary structural representations learned from a single RGB image.

#### ACKNOWLEDGMENT

The work described in this paper was partially supported by grants AoE/E-601/24-N, 16203223, C6029-23G, and C6078-25G from the Research Grants Council of the Hong Kong Special Administrative Region, China. The authors would like to express their sincere gratitude to Prof. Deng-Ping Fan for his valuable suggestions and insightful discussions.

#### REFERENCES

- [1] U. Noppeney, "Perceptual inference, learning, and attention in a multi-sensory world," *Annual Review of Neuroscience*, vol. 44, pp. 449–473, 2021.
- [2] L. Itti, C. Koch, and E. Niebur, "A model of saliency-based visual attention for rapid scene analysis," *IEEE Transactions on Pattern Analysis and Machine Intelligence*, vol. 20, no. 11, pp. 1254–1259, 1998.
- [3] M.-M. Cheng, N. J. Mitra, X. Huang, P. H. Torr, and S.-M. Hu, "Global contrast based salient region detection," *IEEE Transactions on Pattern Analysis and Machine Intelligence*, vol. 37, no. 3, pp. 569–582, 2014.
- [4] S. Khan, I. Ullah, F. Ali, M. Shafiq, Y. Y. Ghadi, and T. Kim, "Deep learning-based marine big data fusion for ocean environment monitoring: Towards shape optimization and salient objects detection," *Frontiers in Marine Science*, vol. 9, p. 1094915, 2023.
- [5] M. Johnson-Roberson, O. Pizarro, and S. Williams, "Saliency ranking for benthic survey using underwater images," in *2010 11th International Conference on Control Automation Robotics & Vision*. IEEE, 2010, pp. 459–466.
- [6] L. Hong, X. Wang, D.-S. Zhang, M. Zhao, and H. Xu, "Vision-based underwater inspection with portable autonomous underwater vehicle: Development, control, and evaluation," *IEEE Transactions on Intelligent Vehicles*, vol. 9, no. 1, pp. 2197–2209, 2024.

- [7] L. Hong, X. Wang, and D. Zhang, "Robust hybrid visual servoing for hovering control of autonomous underwater vehicles in unstructured environments," *Ocean Engineering*, vol. 339, p. 122103, 2025.
- [8] D. Akkaynak and T. Treibitz, "Sea-thru: A method for removing water from underwater images," in *Proceedings of the IEEE/CVF Conference on Computer Vision and Pattern Recognition*, 2019, pp. 1682–1691.
- [9] L. Hong, X. Wang, Z. Xiao, G. Zhang, and J. Liu, "Wsuie: Weakly supervised underwater image enhancement for improved visual perception," *IEEE Robotics and Automation Letters*, vol. 6, no. 4, pp. 8237–8244, 2021.
- [10] J. Jin, Q. Jiang, Q. Wu, B. Xu, and R. Cong, "Underwater salient object detection via dual-stage self-paced learning and depth emphasis," *IEEE Transactions on Circuits and Systems for Video Technology*, 2024.
- [11] Y. LeCun, L. Bottou, Y. Bengio, and P. Haffner, "Gradient-based learning applied to document recognition," *Proceedings of the IEEE*, vol. 86, no. 11, pp. 2278–2324, 1998.
- [12] A. Dosovitskiy, L. Beyer, A. Kolesnikov, D. Weissenborn, X. Zhai, T. Unterthiner, M. Dehghani, M. Minderer, G. Heigold, S. Gelly, J. Uszkoreit, and N. Houlsby, "An image is worth 16x16 words: Transformers for image recognition at scale," in *International Conference on Learning Representations*, 2021.
- [13] A. Borji, M.-M. Cheng, H. Jiang, and J. Li, "Salient object detection: A benchmark," *IEEE Transactions on Image Processing*, vol. 24, no. 12, pp. 5706–5722, 2015.
- [14] T. Zhou, D.-P. Fan, M.-M. Cheng, J. Shen, and L. Shao, "Rgb-d salient object detection: A survey," *Computational Visual Media*, pp. 1–33, 2021.
- [15] Q. Wu, Z. Fu, H. Lin, C. Ma, X. Tu, and X. Ding, "Effisaneet: Pioneering lightweight network for underwater salient object detection," in *Proceedings of the Asian Conference on Computer Vision*, 2024, pp. 1486–1501.
- [16] W. Huang, X. Zhu *et al.*, "A fusion underwater salient object detection based on multi-scale saliency and spatial optimization," *Journal of Marine Science and Engineering*, vol. 11, no. 9, p. 1757, 2023.
- [17] Q. Wu, J. Xie, Z. Fu, X. Tu, Y. Huang, and X. Ding, "Ce<sup>3</sup>usod: Channel-enhanced, efficient, and effective network for underwater salient object detection," *IEEE Journal of Oceanic Engineering*, vol. 50, no. 2, pp. 941–954, 2025.
- [18] G. Yuan, J. Song, and J. Li, "If-usod: Multimodal information fusion interactive feature enhancement architecture for underwater salient object detection," *Information Fusion*, vol. 117, p. 102806, 2025.
- [19] Y. Liu, X. Zhang, K. Zhang, B. Ma, S. Yang, R. Yang, and P. Tan, "Detecting underwater salient objects via self-supervised depth priors and task-driven optimization," *Expert Systems with Applications*, p. 130873, 2025.
- [20] B. Yu, J. Wu, and M. J. Islam, "Udepth: Fast monocular depth estimation for visually-guided underwater robots," in *2023 IEEE International Conference on Robotics and Automation*. IEEE, 2023, pp. 3116–3123.
- [21] L. Hong, X. Wang, G. Zhang, and M. Zhao, "Usod10k: A new benchmark dataset for underwater salient object detection," *IEEE Transactions on Image Processing*, vol. 34, pp. 1602–1615, 2025.
- [22] W. Ji, J. Li, S. Yu, M. Zhang, Y. Piao, S. Yao, Q. Bi, K. Ma, Y. Zheng, H. Lu, and L. Cheng, "Calibrated rgb-d salient object detection," in *Proceedings of the IEEE/CVF Conference on Computer Vision and Pattern Recognition*, June 2021, pp. 9471–9481.
- [23] W. Ji, J. Li, M. Zhang, Y. Piao, and H. Lu, "Accurate rgb-d salient object detection via collaborative learning," in *Proceedings of the European Conference on Computer Vision*, 2020, pp. 52–69.
- [24] X. Qin, Z. Zhang, C. Huang, C. Gao, M. Dehghan, and M. Jagersand, "Basnet: Boundary-aware salient object detection," in *Proceedings of the IEEE/CVF Conference on Computer Vision and Pattern Recognition*, 2019, pp. 7479–7489.
- [25] Z. Tu, Y. Ma, C. Li, J. Tang, and B. Luo, "Edge-guided non-local fully convolutional network for salient object detection," *IEEE Transactions on Circuits and Systems for Video Technology*, vol. 31, no. 2, pp. 582–593, 2020.
- [26] J. Zhao, J.-J. Liu, D.-P. Fan, Y. Cao, J. Yang, and M.-M. Cheng, "Egnet: Edge guidance network for salient object detection," in *2019 IEEE/CVF International Conference on Computer Vision*, 2019, pp. 8778–8787.
- [27] J. Su, J. Li, Y. Zhang, C. Xia, and Y. Tian, "Selectivity or invariance: Boundary-aware salient object detection," in *Proceedings of the IEEE/CVF International Conference on Computer Vision*, 2019, pp. 3799–3808.
- [28] J. Wei, S. Wang, Z. Wu, C. Su, Q. Huang, and Q. Tian, "Label decoupling framework for salient object detection," in *Proceedings of the IEEE/CVF Conference on Computer Vision and Pattern Recognition*, 2020, pp. 13 025–13 034.

- [29] Y. Wei, Y. Wang, S. Yan, T. Wang, Z. Wang, W. Sun, Y. Zhao, and X. Xue, "Csunet: Contour-sensitive underwater salient object detection," in *Proceedings of the 6th ACM Multimedia Asia*, 2024, pp. 78:1–78:7.
- [30] S. Ren, W. Liu, J. Jiao, G. Han, and S. He, "Edge distraction-aware salient object detection," *IEEE MultiMedia*, vol. 30, no. 3, pp. 63–73, 2023.
- [31] S. Grossberg, "Filling-in the forms: Surface and boundary interactions in visual cortex," in *Filling-in: From Perceptual Completion to Skill Learning*, L. Pessoa and P. D. Weerd, Eds. New York: Oxford University Press, 2003, pp. 13–37.
- [32] S. Kastner and L. G. Ungerleider, "Mechanisms of visual attention in the human cortex," *Annual Review of Neuroscience*, vol. 23, pp. 315–341, 2000.
- [33] Z. Chen, H. Gao, Z. Zhang, H. Zhou, X. Wang, and Y. Tian, "Underwater salient object detection by combining 2d and 3d visual features," *Neurocomputing*, vol. 391, pp. 249–259, 2020.
- [34] W. Wang, Q. Lai, H. Fu, J. Shen, H. Ling, and R. Yang, "Salient object detection in the deep learning era: An in-depth survey," *IEEE Transactions on Pattern Analysis and Machine Intelligence*, vol. 44, no. 6, pp. 3239–3259, 2021.
- [35] Y. Liu, X. Zhang, J. Zhu, B. Ma, Y. Duan, and P. Tan, "Hdanet: Enhancing underwater salient object detection with physics-inspired multimodal joint learning," *IEEE Transactions on Geoscience and Remote Sensing*, 2025.
- [36] W. Zhou, B. Tang, R. Cong, and Q. Jiang, "Turbidity-similarity decoupling: Feature-consistent mutual learning for underwater salient object detection," *IEEE Transactions on Image Processing*, pp. 1–1, 2026.
- [37] Y.-T. Peng, Y.-C. Lin, W.-Y. Peng, and C.-Y. Liu, "Blurriness-guided underwater salient object detection and data augmentation," *IEEE Journal of Oceanic Engineering*, vol. 49, no. 3, pp. 1089–1103, 2024.
- [38] M. Zha, G. Wang, Y. Pei, T. Li, X. Tang, C. Li, Y. Yang, and H. T. Shen, "Heterogeneous experts and hierarchical perception for underwater salient object detection," *IEEE Transactions on Image Processing*, 2025.
- [39] J.-J. Liu, Q. Hou, M.-M. Cheng, J. Feng, and J. Jiang, "A simple pooling-based design for real-time salient object detection," in *Proceedings of the IEEE/CVF Conference on Computer Vision and Pattern Recognition*, 2019, pp. 3917–3926.
- [40] Y. Pang, X. Zhao, L. Zhang, and H. Lu, "Multi-scale interactive network for salient object detection," in *2020 IEEE/CVF Conference on Computer Vision and Pattern Recognition*, 2020, pp. 9410–9419.
- [41] J. Wei, S. Wang, and Q. Huang, "F<sup>3</sup>net: fusion, feedback and focus for salient object detection," in *Proceedings of the AAAI conference on artificial intelligence*, vol. 34, no. 07, 2020, pp. 12 321–12 328.
- [42] Z. Wu, L. Su, and Q. Huang, "Stacked cross refinement network for edge-aware salient object detection," in *Proceedings of the IEEE/CVF International Conference on Computer Vision*, 2019, pp. 7264–7273.
- [43] A. Paszke, S. Gross, F. Massa, A. Lerer, J. Bradbury, G. Chanan, T. Killeen, Z. Lin, N. Gimelshein, L. Antiga *et al.*, "Pytorch: An imperative style, high-performance deep learning library," *Advances in neural information processing systems*, vol. 32, pp. 8026–8037, 2019.
- [44] W. Wang, E. Xie, X. Li, D.-P. Fan, K. Song, D. Liang, T. Lu, P. Luo, and L. Shao, "Pvt v2: Improved baselines with pyramid vision transformer," *Computational visual media*, vol. 8, no. 3, pp. 415–424, 2022.
- [45] D. P. Kingma and J. Ba, "Adam: A method for stochastic optimization," *arXiv preprint arXiv:1412.6980*, 2014.
- [46] M. J. Islam, R. Wang, and Y. Sattar, "Svam: Saliency-guided visual attention modeling by autonomous underwater robots," in *18th Robotics: Science and Systems, RSS 2022*. MIT Press Journals, 2022.
- [47] D.-P. Fan, M.-M. Cheng, Y. Liu, T. Li, and A. Borji, "Structure-measure: A new way to evaluate foreground maps," in *2017 IEEE International Conference on Computer Vision*, 2017, pp. 4558–4567.
- [48] D.-P. Fan, C. Gong, Y. Cao, B. Ren, M.-M. Cheng, and A. Borji, "Enhanced-alignment measure for binary foreground map evaluation," in *Proceedings of the 27th International Joint Conference on Artificial Intelligence*, 2018, pp. 698–704.
- [49] R. Achanta, S. Hemami, F. Estrada, and S. Susstrunk, "Frequency-tuned salient region detection," in *2009 IEEE Conference on Computer Vision and Pattern Recognition*, 2009, pp. 1597–1604.
- [50] F. Perazzi, P. Krähenbühl, Y. Pritch, and A. Hornung, "Saliency filters: Contrast based filtering for salient region detection," in *2012 IEEE Conference on Computer Vision and Pattern Recognition*, 2012, pp. 733–740.
- [51] B. Wang, Q. Chen, M. Zhou, Z. Zhang, and K. Gai, "Progressive feature polishing network for salient object detection," *Proceedings of the AAAI Conference on Artificial Intelligence*, vol. 34, no. 7, pp. 12 128–12 135, 2020.
- [52] J. Zhao, Y. Zhao, J. Li, and X. Chen, "Is depth really necessary for salient object detection?" in *Proceedings of the 28th ACM International Conference on Multimedia*, 2020, pp. 1745–1754.
- [53] M. Ma, C. Xia, and J. Li, "Pyramidal feature shrinking for salient object detection," in *Proceedings of the AAAI Conference on Artificial Intelligence*, vol. 35, no. 3, 2021, pp. 2311–2318.
- [54] Y. Piao, J. Wang, M. Zhang, and H. Lu, "Mfnet: Multi-filter directive network for weakly supervised salient object detection," in *Proceedings of the IEEE/CVF International Conference on Computer Vision*, 2021, pp. 4136–4145.
- [55] Z. Zhao, C. Xia, C. Xie, and J. Li, "Complementary trilateral decoder for fast and accurate salient object detection," in *Proceedings of the 29th ACM International Conference on Multimedia*, 2021, pp. 4967–4975.
- [56] S. Yang, W. Lin, G. Lin, Q. Jiang, and Z. Liu, "Progressive self-guided loss for salient object detection," *IEEE Transactions on Image Processing*, vol. 30, pp. 8426–8438, 2021.
- [57] N. Liu, N. Zhang, K. Wan, L. Shao, and J. Han, "Visual saliency transformer," in *Proceedings of the IEEE/CVF International Conference on Computer Vision*, October 2021, pp. 4722–4732.
- [58] M.-M. Cheng, S.-H. Gao, A. Borji, Y.-Q. Tan, Z. Lin, and M. Wang, "A highly efficient model to study the semantics of salient object detection," *IEEE Transactions on Pattern Analysis and Machine Intelligence*, 2022.
- [59] G. Zhu, J. Li, and Y. Guo, "Separate first, then segment: An integrity segmentation network for salient object detection," *Pattern Recognition*, vol. 150, p. 110328, 2024.
- [60] Y. Qiu, Y. Liu, L. Zhang, H. Lu, and J. Xu, "Boosting salient object detection with transformer-based asymmetric bilateral u-net," *IEEE Transactions on Circuits and Systems for Video Technology*, vol. 34, no. 4, 2024.
- [61] Y. Mao, J. Zhang, Z. Wan, X. Tian, A. Li, Y. Lv, and Y. Dai, "Generative transformer for accurate and reliable salient object detection," *IEEE Transactions on Circuits and Systems for Video Technology*, vol. 35, no. 2, pp. 1041–1054, 2025.
- [62] Z. Su, L. Liu, M. Müller, J. Zhang, D. Wofk, M.-M. Cheng, and M. Pietikäinen, "Rapid salient object detection with difference convolutional neural networks," *IEEE Transactions on Pattern Analysis and Machine Intelligence*, 2025.
- [63] K. Fu, D.-P. Fan, G.-P. Ji, and Q. Zhao, "Jl-dcf: Joint learning and densely-cooperative fusion framework for rgb-d salient object detection," in *Proceedings of the IEEE/CVF conference on Computer Vision and Pattern Recognition*, 2020, pp. 3052–3062.
- [64] J. Zhang, D.-P. Fan, Y. Dai, S. Anwar, F. Sadat Saleh, T. Zhang, and N. Barnes, "Uc-net: Uncertainty inspired rgb-d saliency detection via conditional variational autoencoders," in *Proceedings of the IEEE conference on Computer Vision and Pattern Recognition*, 2020.
- [65] N. Liu, N. Zhang, L. Shao, and J. Han, "Learning selective mutual attention and contrast for rgb-d saliency detection," *IEEE Transactions on Pattern Analysis and Machine Intelligence*, vol. 44, no. 12, pp. 9026–9042, 2021.
- [66] D.-P. Fan, Y. Zhai, A. Borji, J. Yang, and L. Shao, "Bbs-net: Rgb-d salient object detection with a bifurcated backbone strategy network," in *European Conference on Computer Vision*. Springer, 2020, pp. 275–292.
- [67] X. Zhao, L. Zhang, Y. Pang, H. Lu, and L. Zhang, "A single stream network for robust and real-time rgb-d salient object detection," in *European Conference on Computer Vision*. Springer, 2020, pp. 646–662.
- [68] T. Zhou, H. Fu, G. Chen, Y. Zhou, D.-P. Fan, and L. Shao, "Specificity-preserving rgb-d saliency detection," in *Proceedings of the IEEE/CVF International Conference on Computer Vision*, 2021, pp. 4681–4691.
- [69] G. Li, Z. Liu, M. Chen, Z. Bai, W. Lin, and H. Ling, "Hierarchical alternate interaction network for rgb-d salient object detection," *IEEE Transactions on Image Processing*, vol. 30, pp. 3528–3542, 2021.
- [70] Z. Liu, Y. Wang, Z. Tu, Y. Xiao, and B. Tang, "Tritransnet: Rgb-d salient object detection with a triplet transformer embedding network," *Proceedings of the 29th ACM International Conference on Multimedia*, 2021.
- [71] D.-P. Fan, Z. Lin, Z. Zhang, M. Zhu, and M.-M. Cheng, "Rethinking rgb-d salient object detection: Models, data sets, and large-scale benchmarks," *IEEE Transactions on Neural Networks and Learning Systems*, vol. 32, no. 5, pp. 2075–2089, 2020.

- [72] W. Zhang, Y. Jiang, K. Fu, and Q. Zhao, "Bts-net: Bi-directional transfer-and-selection network for rgb-d salient object detection," in *2021 IEEE International Conference on Multimedia and Expo*. IEEE, 2021, pp. 1–6.
- [73] C. Zhang, R. Cong, Q. Lin, L. Ma, L. Feng, Y. Zhao, and S. Kwong, "Cross-modality discrepant interaction network for RGB-D salient object detection," in *Proceedings of the 29th ACM International Conference on Multimedia*. ACM, 2021.
- [74] R. Cong, Q. Lin, C. Zhang, C. Li, X. Cao, Q. Huang, and Y. Zhao, "Cir-net: Cross-modality interaction and refinement for rgb-d salient object detection," *IEEE Transactions on Image Processing*, vol. 31, 2022.
- [75] Z. Wu, G. Allibert, F. Meriaudeau, C. Ma, and C. Demonceaux, "Hid-net: Rgb-d salient object detection via hierarchical depth awareness," *IEEE Transactions on Image Processing*, vol. 32, 2023.
- [76] R. Cong, H. Liu, C. Zhang, W. Zhang, F. Zheng, R. Song, and S. Kwong, "Point-aware interaction and cnn-induced refinement network for rgb-d salient object detection," in *Proceedings of the 31st ACM International Conference on Multimedia*, 2023.
- [77] F. Sun, P. Ren, B. Yin, F. Wang, and H. Li, "Catnet: A cascaded and aggregated transformer network for rgb-d salient object detection," *IEEE Transactions on Multimedia*, vol. 26, 2024.
- [78] S. Duan, X. Yang, N. Wang, and X. Gao, "Lightweight rgb-d salient object detection from a speed-accuracy tradeoff perspective," *IEEE Transactions on Image Processing*, vol. 34, pp. 2529–2543, 2025.
- [79] H. Li, G. Lin, Z. Li, S. Kwong, and R. Cong, "Fscdiff: Frequency-spatial entangled conditional diffusion model for underwater salient object detection," in *Proceedings of the 33rd ACM International Conference on Multimedia*, 2025, pp. 8379–8388.
- [80] K. He, X. Zhang, S. Ren, and J. Sun, "Deep residual learning for image recognition," in *Proceedings of the IEEE Conference on Computer Vision and Pattern Recognition*, 2016, pp. 770–778.
- [81] Z. Liu, H. Mao, C.-Y. Wu, C. Feichtenhofer, T. Darrell, and S. Xie, "A convnet for the 2020s," in *Proceedings of the IEEE/CVF Conference on Computer Vision and Pattern Recognition*, 2022, pp. 11 976–11 986.
- [82] Z. Liu, H. Hu, Y. Lin, Z. Yao, Z. Xie, Y. Wei, J. Ning, Y. Cao, Z. Zhang, L. Dong *et al.*, "Swin transformer v2: Scaling up capacity and resolution," in *Proceedings of the IEEE/CVF Conference on Computer Vision and Pattern Recognition*, 2022, pp. 12 009–12 019.
- [83] D. Zhang, H. Tian, and J. Han, "Few-cost salient object detection with adversarial-paced learning," *Advances in Neural Information Processing Systems*, vol. 33, pp. 12 236–12 247, 2020.
- [84] Y. Liu, Y.-C. Gu, X.-Y. Zhang, W. Wang, and M.-M. Cheng, "Lightweight salient object detection via hierarchical visual perception learning," *IEEE transactions on Cybernetics*, vol. 51, no. 9, pp. 4439–4449, 2020.
- [85] B. Xu, H. Liang, R. Liang, and P. Chen, "Locate globally, segment locally: A progressive architecture with knowledge review network for salient object detection," in *Proceedings of the AAAI Conference on Artificial Intelligence*, vol. 35, no. 4, 2021, pp. 3004–3012.
- [86] Y. Liu, X.-Y. Zhang, J.-W. Bian, L. Zhang, and M.-M. Cheng, "Samnet: Stereoscopically attentive multi-scale network for lightweight salient object detection," *IEEE Transactions on Image Processing*, vol. 30, pp. 3804–3814, 2021.
- [87] Z. Wu, S. Li, C. Chen, H. Qin, and A. Hao, "Salient object detection via dynamic scale routing," *IEEE Transactions on Image Processing*, vol. 31, pp. 6649–6663, 2022.
- [88] Y.-H. Wu, Y. Liu, L. Zhang, M.-M. Cheng, and B. Ren, "Edn: Salient object detection via extremely-downsampled network," *IEEE Transactions on Image Processing*, vol. 31, pp. 3125–3136, 2022.
- [89] Y. Liu, D. Zhang, Q. Zhang, and J. Han, "Part-object relational visual saliency," *IEEE Transactions on Pattern Analysis and Machine Intelligence*, vol. 44, no. 7, pp. 3688–3704, 2022.
- [90] H. Mei, Y. Liu, Z. Wei, D. Zhou, X. Wei, Q. Zhang, and X. Yang, "Exploring dense context for salient object detection," *IEEE Transactions on Circuits and Systems for Video Technology*, vol. 32, no. 3, pp. 1378–1389, 2022.
- [91] C. Zhang, S. Gao, D. Mao, and Y. Zhou, "Dhnet: Salient object detection with dynamic scale-aware learning and hard-sample refinement," *IEEE Transactions on Circuits and Systems for Video Technology*, vol. 32, no. 11, pp. 7772–7782, 2022.
- [92] Y. Wang, R. Wang, X. Fan, T. Wang, and X. He, "Pixels, regions, and objects: Multiple enhancement for salient object detection," in *2023 IEEE/CVF Conference on Computer Vision and Pattern Recognition*, 2023, pp. 10031–10040.
- [93] M. Ma, C. Xia, C. Xie, X. Chen, and J. Li, "Boosting broader receptive fields for salient object detection," *IEEE Transactions on Image Processing*, vol. 32, pp. 1026–1038, 2023.
- [94] M. Zhuge, D.-P. Fan, N. Liu, D. Zhang, D. Xu, and L. Shao, "Salient object detection via integrity learning," *IEEE Transactions on Pattern Analysis and Machine Intelligence*, vol. 45, no. 3, pp. 3738–3752, 2023.
- [95] J. Zhu, X. Zhang, X. Fang, Y. Wang, P. Tan, and J. Liu, "Perception-and-regulation network for salient object detection," *IEEE Transactions on Multimedia*, vol. 25, pp. 6525–6537, 2023.
- [96] Z. Luo, N. Liu, W. Zhao, X. Yang, D. Zhang, D.-P. Fan, F. Khan, and J. Han, "Vscore: General visual salient and camouflaged object detection with 2d prompt learning," in *Proceedings of the IEEE/CVF conference on Computer Vision and Pattern Recognition*, 2024, pp. 17 169–17 180.
- [97] N. Liu, Z. Luo, N. Zhang, and J. Han, "Vst++: Efficient and stronger visual saliency transformer," *IEEE Transactions on Pattern Analysis and Machine Intelligence*, vol. 46, no. 11, pp. 7300–7316, 2024.
- [98] L. Zhang and Q. Zhang, "Salient object detection with edge-guided learning and specific aggregation," *IEEE Transactions on Circuits and Systems for Video Technology*, vol. 34, no. 1, pp. 534–548, 2024.
- [99] C. Hao, Z. Yu, X. Liu, J. Xu, H. Yue, and J. Yang, "A simple yet effective network based on vision transformer for camouflaged object and salient object detection," *IEEE Transactions on Image Processing*, vol. 34, pp. 608–622, 2025.
- [100] J. He, K. Fu, X. Liu, and Q. Zhao, "Samba: A unified mamba-based framework for general salient object detection," in *Proceedings of the Computer Vision and Pattern Recognition Conference*, 2025, pp. 25 314–25 324.
- [101] L. Wang, H. Lu, Y. Wang, M. Feng, D. Wang, B. Yin, and X. Ruan, "Learning to detect salient objects with image-level supervision," in *2017 IEEE Conference on Computer Vision and Pattern Recognition*, 2017, pp. 3796–3805.
- [102] C. Yang, L. Zhang, H. Lu, X. Ruan, and M.-H. Yang, "Saliency detection via graph-based manifold ranking," in *Proceedings of the IEEE Conference on Computer Vision and Pattern Recognition*, 2013, pp. 3166–3173.
- [103] G. Li and Y. Yu, "Visual saliency based on multiscale deep features," in *Proceedings of the IEEE conference on Computer Vision and Pattern Recognition*, 2015, pp. 5455–5463.
- [104] Q. Yan, L. Xu, J. Shi, and J. Jia, "Hierarchical saliency detection," in *Proceedings of the IEEE conference on Computer Vision and Pattern Recognition*, 2013, pp. 1155–1162.
- [105] V. Movahedi and J. H. Elder, "Design and perceptual validation of performance measures for salient object segmentation," in *2010 IEEE computer society conference on Computer Vision and Pattern Recognition-workshops*. IEEE, 2010, pp. 49–56.
- [106] Y. Li, X. Hou, C. Koch, J. M. Rehg, and A. L. Yuille, "The secrets of salient object segmentation," in *2014 IEEE Conference on Computer Vision and Pattern Recognition*, 2014, pp. 280–287.